Optimum satellite remote sensing of the marine carbonate system using empirical algorithms in the Global Ocean, the Greater Caribbean, the Amazon Plume and the Bay of Bengal

Peter E. Land and Helen S. Findlay, Plymouth Marine Laboratory, Prospect Place, West Hoe, Plymouth, PL1 3DH, UK

Jamie D. Shutler, Ian G.C. Ashton and Thomas Holding, University of Exeter, Penryn, Cornwall, TR10 9FE, UK

Antoine Grouazel, Fanny Girard-Ardhuin, Nicolas Reul, Jean-Francois Piolle, Bertrand Chapron and Yves Quilfen, Ifremer, University Brest, CNRS, IRD, Laboratoire d'Océanographie Physique et Spatiale (LOPS), IUEM, F-29280, Brest, France.

Richard G.J. Bellerby, SKLEC-NIVA Centre for Marine and Coastal Research, State Key Laboratory for Estuarine and Coastal Research, East China Normal University Zhongshan N. Road, 3663, Shanghai 200062, China; and Norwegian Institute for Water Research, Thormølensgate 53D, N-5006, Bergen, Norway.

Punyasloke Bhadury, Department of Biological Sciences, Indian Institute of Science Education and Research Kolkata, Mohanpur 741 246, West Bengal, India

Joseph Salisbury and Douglas Vandemark, Ocean Processes Analysis Laboratory, University of New Hampshire, Durham, New Hampshire, 3824, United States

Roberto Sabia, Telespazio-Vega U.K. for European Space Agency (ESA), ESRIN, Frascati, Italy

Corresponding author: P. E. Land, Plymouth Marine Laboratory, Prospect Place, West Hoe, Plymouth, PL1 3DH, UK. (peland@pml.ac.uk)

Research highlights

- Satellite salinity measurements enable estimation of surface carbonate parameters.
- Uncertainties within these observation-based estimates are well characterized.
- Monthly satellite salinity and temperature allows synoptic monitoring.
- Satellite observations allow study of seasonal, interannual and episodic variations

Abstract

Improving our ability to monitor ocean carbonate chemistry has become a priority as the ocean continues to absorb carbon dioxide from the atmosphere. This long-term uptake is reducing the ocean pH; a process commonly known as ocean acidification. The use of satellite Earth Observation has not yet been thoroughly explored as an option for routinely observing surface ocean carbonate chemistry, although its potential has been highlighted. We demonstrate the suitability of using empirical algorithms to calculate total alkalinity (A_T) and total dissolved inorganic carbon (C_T), assessing the relative performance of satellite, interpolated *in situ*, and climatology datasets in reproducing the wider spatial patterns of these two variables. Both A_T and C_T *in situ* data are reproducible, both regionally and globally, using salinity and temperature datasets, with satellite observed salinity from Aquarius and SMOS providing performance comparable to other datasets for the majority of case studies. Global root mean squared difference (RMSD) between *in situ* validation data and satellite estimates is 17 μmol kg^{-1} with bias < 5 μmol kg^{-1} for A_T and 30 μmol kg^{-1} with bias < 10 μmol kg^{-1} for C_T. This analysis demonstrates that satellite sensors provide a credible solution for monitoring surface synoptic scale A_T and C_T. It also enables the first demonstration of observation-based synoptic scale A_T and C_T temporal mixing in the Amazon plume for 2010-2016, complete with a robust estimation of their uncertainty.

Keywords

Carbonate chemistry; Earth observation; Ocean acidification; Total alkalinity; Dissolved inorganic carbon; SMOS; Aquarius; CORA; HadGEM2-ES

1. Introduction

The oceans play an important role in absorbing carbon (e.g. Sabine et al., 2004), and the increase in CO_2 emitted into the atmosphere as a result of anthropogenic activities has resulted in an increase in CO_2 uptake by the oceans (Caldeira and Wickett, 2005; Sabine et al., 2004; Takahashi et al., 2009). This long-term absorption results in a shift in ocean carbonate chemistry, which has the potential to alter biogeochemical cycles and ecosystem function in the future (Raven et al., 2005; Kroeker et al. 2013). As a result of the decrease in ocean pH arising from these shifts (often termed Ocean Acidification), this change in ocean carbonate chemistry has received increasing scientific and political attention over the past decade. This has led to questions about the magnitude and importance of spatial and temporal ocean carbon variability, as well as how to monitor ongoing change at global and regional scales. To-date, carbonate system monitoring has been primarily from ship- and field-based observations that provide relatively disparate and sparse datasets of carbonate chemistry parameters in both space and time. To expand capabilities, state-of-the-art autonomous *in situ* tools are needed (Byrne, 2014). Recent advances include pH sensors on biogeochemical floats (e.g. Johnson *et al.,* 2017), and sensors to observe multiple carbonate system parameters *in situ* are now in development (Bushinsky *et al.,* 2019). One such advancement is utilizing Earth Observation (EO) satellites to provide wider spatial and temporal coverage of surface carbonate chemistry observations, with the aim of detecting features and characterizing dynamics that are difficult to resolve using *in situ* datasets (Land *et al.,* 2015; Salisbury *et al.,* 2015; Fine *et al.*, 2017). Currently, there are just two satellites in orbit that are specifically designed to support global carbon cycle research (The US NASA Orbiting Carbon Observatory OCO-2 (Osterman et al. 2016), and the Chinese Tansat; Yang et al. 2018), but their focus is to observe and monitor atmospheric CO_2. However, there is a suite of ocean observing satellite sensor datasets that could be used, through exploitation of

empirical relationships, to provide measures of marine carbonate chemistry parameters that include total alkalinity (A_T), total dissolved inorganic carbon (C_T), partial pressure of CO_2 in seawater (pCO_2) and pH (Gledhill *et al.,* 2009).

These four primary variables allow the ocean carbonate system to be investigated. In principle, knowledge of at least two of these four, in conjunction with temperature, salinity and pressure, allows the remaining variables to be calculated (Dickson and Riley, 1978). The relationships between these variables are principally driven by thermodynamics; temperature, pressure and salinity are therefore fundamentally associated with the carbonate system (Dickson, 2007). Furthermore, salinity is a significant driver of the ionic composition of seawater and hence has a strong relationship with A_T (Millero *et al.,* 1998). In addition to these physical controls on the carbonate system, the variables can be influenced by other chemical processes, including weathering and carbonate formation/dissolution (Friis *et al.,* 2003), and biological processes such as primary production, respiration, calcification and remineralization (Smith *et al.,* 1975). With this knowledge it is possible to determine how the carbonate system variables vary in relation to factors such as temperature, salinity, nitrate or chlorophyll (the latter two as proxies for biological processes). These relationships take the form of empirical algorithms, which can be used to derive the respective carbonate system variable, and have been developed within a number of global and regional studies, e.g. Takahashi *et al.* (2013); Lee *et al.* (2006); Lee *et al.* (2000); Sasse *et al.* (2013); Cai *et al.* (2010); Lefèvre *et al.* (2010); Bonou *et al.* (2016); see Land *et al.* (2015) and references therein.

Although initially developed from *in situ* datasets, these empirical algorithms could potentially be forced with inputs from other sources, such as satellite observations or

105 climatologies to yield observation-based carbon system observations. Here we conduct a first
106 assessment of four global algorithms for A_T and three for C_T, utilizing different combinations
107 of satellite, interpolated *in situ* and climatology datasets as input. We then evaluate their
108 output using independent *in situ* measurements of A_T and C_T. As a baseline comparison, we
109 evaluate estimates of A_T and C_T from an Earth System model. In addition to the global
110 algorithms, we also assess three regional A_T and two regional C_T algorithms. We aim to
111 demonstrate algorithm suitability both globally and for regional case studies (the Caribbean,
112 the Amazon plume and the Bay of Bengal), and to assess the performance of these different
113 approaches, particularly the relevance of satellite datasets, in being able to reproduce the *in*
114 *situ* patterns of these two carbonate system variables in surface waters.
115
116 **2. Materials and methods**
117 ***2.1. Published algorithms***
118 The four global algorithms used here for A_T are from Lee *et al.* (2006) (hereafter referred to
119 as L06), Takahashi and Sutherland (2013) (hereafter referred to as TS13) and Sasse et al
120 (2013) (domain-based and global algorithms, hereafter referred to as S13 and S13g). L06
121 separated the oceans into five domains and used an optimal polynomial fit to A_T data,
122 resulting in a relationship with sea surface salinity (SSS) and sea surface temperature (SST)
123 for each region. TS13 took this a step further using a larger combination of datasets to
124 separate the oceans into 33 domains. Instead of using SST and SSS, TS13 assessed potential
125 alkalinity relationship with SSS, where potential alkalinity is A_T plus nitrate concentration
126 (NO_3), which corrects A_T for the effect of changes in NO_3 caused by net community
127 utilization. Sasse et al (2013) used multiple linear regression to relate domain and global A_T
128 to SST, SSS, SSS^2, dissolved oxygen (DO), silicate (Si) and phosphate (PO_4). The three
129 regional A_T algorithms are all linear relationships with SSS using data from the Amazon

130 plume and Caribbean (Cai *et al.,* 2010; Lefèvre *et al.,* 2010). Two other regional algorithms
131 (Cooley *et al.,* 2007; Ternon *et al.,* 2000) were considered, but were not used here as results
132 differed only marginally from Lefèvre *et al.,* (2010) and they used much of the same training
133 data.
134
135 The three global C_T algorithms that we used are from Lee *et al.* (2000) (hereafter referred to
136 as L00) and Sasse *et al.* (2013) (domain-based and global algorithms, hereafter referred to as
137 S13 and S13g). L00 found C_T normalized to salinity 35 on the Practical Salinity Scale and
138 year 1990, ($nC_T = C_T \times 35 / SSS +$ (year – 1990 between 30°S and 30°N)), to be strongly
139 correlated with SST and NO_3, and conducted optimal polynomial fitting for C_T to domain
140 data, giving a total of 12 regionally parameterized equations. Sasse *et al.* (2013) used
141 multiple linear regression to relate domain and global C_T to SST, SSS, DO, NO_3, Si and PO_4.
142 The two regional C_T algorithms are both linear relationships with SSS using data from the
143 Amazon plume (Lefèvre *et al.*, 2010; Bonou *et al.,* 2016). The same two regional studies as
144 for A_T (Cooley *et al.,* 2007; Ternon *et al.,* 2000) were considered for C_T, but again results
145 differed only marginally from those of Lefèvre *et al.*, (2010) and so they were not used.
146 In all cases, extrapolation of algorithms beyond the range for which they were calibrated is
147 questionable, and this is especially true of nonlinear algorithms. To avoid this, we did not use
148 any algorithm outside its specified range of applicability, or more than one SSS unit or SST
149 degree outside its calibration range if a range of applicability is not specified. Table 1
150 summarises the algorithm choices and dependences. Additional details on each empirical
151 relationship for all algorithms are provided in Supporting Information Text S1.
152

153 ### *2.2. Round-robin comparison*

Four case study regions were used in a round-robin comparison of the algorithms: the global ocean, the Caribbean (14°N to 30°N, 90°W to 60°W for compatibility with Gledhill *et al.* (2008)), the Amazon plume (2°S to 22°N, 70°W to 32°W), and the Bay of Bengal (5°N to 24°N, 78°E to 96°E, using the Bay of Bengal International Hydrographic Office Sea Area (International Hydrographic Organization, 1953)). These case studies were chosen as areas that are potentially challenging for this assessment and are discussed in more detail in Land *et al.,* (2015). The Amazon region was chosen to enclose the region of freshening contiguous with the mouth of the Amazon with any monthly satellite SSS < 35, with an eastern boundary at 32°W, beyond which rain freshening dominates the Amazon plume (Ibánhez *et al.,* 2016). The region defined also includes many points with SSS > 35. To investigate the effect of these points, we also defined a low-salinity Amazon region where data with *in situ* SSS > 35 were excluded.

Each algorithm was tested using input data for each forcing factor (SSS, SST, NO_3, DO, Si and/or PO_4) from a range of data sources and all possible combinations of inputs were included in the round-robin comparison. The input data for the empirical algorithms were:

1) Monthly mean satellite observed data from the Soil Moisture and Ocean Salinity (SMOS) satellite [SSS 2010-2017 CATDS-IFR-CEC-v02] (Reul *et al.,* 2015), the Aquarius satellite [SSS 2011-2015, Version 5] (Le Vine *et al.,* 2014), and the Climate Change Initiative (CCI) [SST 1991-2010] (Merchant *et al.,* 2012);

2) *In situ* re-analysis data from the Coriolis Ocean Re-Analysis (CORA v4.3) database [SSS, SST 1990-2012] (Cabanes *et al.,* 2013);

3) Monthly climatology data from the World Ocean Atlas (WOA) dataset [SSS, SST, nitrate, DO, Si, PO_4] (Garcia *et al.,* 2010);

178 Note that WOA 'nitrate' is actually nitrate + nitrite (NO_3 + NO_2). However, NO_2 typically
179 has a concentration at least an order of magnitude lower than NO_3, and so this discrepancy is
180 neglected. The previously mentioned baseline comparison dataset were A_T and C_T output
181 from the HadGEM2-ES global Earth system model, 1972-2020 (Jones *et al.,* 2011) (hereafter
182 referred to as HG2).
183 All data were binned spatially to a 1°x1° grid and temporally to monthly intervals (henceforth
184 referred to as monthly data). The multi-year CORA, satellite and HG2 data were also each
185 combined to form monthly climatologies (climatological data). Only 1°x1° grid cells with at
186 least two values were used to calculate climatological data. Details of all of these input
187 datasets are provided in Table 2.
188
189 The binned A_T or C_T from each algorithm and input, herein referred to as 'output', and the
190 binned output from HG2 were all evaluated (validated) against binned *in situ* data of the
191 respective carbonate parameter. Data from the Global Data Analysis Project Version 2
192 (GLODAPv2, 1972-2013) (Olsen *et al.,* 2016) were the primary *in situ* evaluation
193 (validation) data used for both A_T and C_T evaluations, along with some additional regional *in*
194 *situ* data (see Table 3). The GLODAPv2 dataset is a community compiled, merged and
195 internally consistent global dataset. In all cases of *in situ* data, the mean measurement in the
196 top 10 m water depth was used.
197
198 Following (Sasse et al. 2013), we attempted to separate the effects of terrigenous influences
199 and sediment resuspension on the biogeochemistry of coastal waters from open ocean
200 carbonate chemistry by calculating the minimum depth within each cell using the
201 GEBCO_08 one-minute grid (www. gebco.net/

data_and_products/gridded_bathymetry_data/gebco_one_minute_grid/, downloaded on December 14th, 2009) and repeating our analysis using only grid cells with minimum depth greater than 500 m. Again following (Sasse et al. 2013), we further separated terrigenous effects by calculating the minimum distance from the nearest coast within each cell using (https://oceancolor.gsfc.nasa.gov/docs/distfromcoast/, downloaded on October 5th, 2018) and repeated the analysis using only grid cells with both a minimum depth greater than 500 m and a minimum distance greater than 300 km. All three sets of results are included in Supplementary Information, but only data with both masks applied are presented here.

2.3. Statistical measures

2.3.1 Data uncertainties

The GLODAPv2 analysis (Olsen *et al.,* 2016), the chosen reference validation dataset, includes an estimate of the maximum bias that exists between different instruments determined via a crossover analysis as 4 and 6 μmol kg^{-1} for C_T and A_T respectively. Whereas a full uncertainty budget (i.e. a type A uncertainty estimate (BIPM, 2008) comprising a combination of bias and standard deviation of all measurements against a traceable standard) are not provided. Therefore in the absence of all components of the uncertainty information we assume nominal uncertainties of 0.5% for all *in situ* A_T and C_T (Bockmon *et al.,* 2015). It should be noted that due to relatively recent improvements in quality control we would expect older *in situ* measurements to have greater uncertainties and more recent measurements to have lesser, though this variation is difficult to quantify. For interest, the GLODAPv2 bias estimate stated above for a mean global A_T of 2450 μmol kg^{-1} gives a potential bias around 0.2%. Uncertainties in the input (forcing) data (SST, SSS, NO_3 and HG2 A_T and C_T) were not included in our analysis, since these are unknown for many of the input datasets. For interest only, the reported uncertainty in SMOS SSS is below ±0.3 for a 30

227 day average over a 100 × 100 km open ocean area (Reul *et al.,* 2012; Reul *et al.,* 2014) and
228 can be below ±0.2 for an 18 day average (Boutin *et al.,* 2018) or in certain evaporation-
229 dominated regions, and for Aquarius SSS it is ±0.17 for a monthly average over a 150 × 150
230 km open ocean area (Lagerloef *et al.,* 2015). Uncertainty in CCI SST is between ±0.1 and
231 ±0.15 K (Merchant *et al.,* 2014). However, we could find no uncertainty estimates for the
232 CORA, WOA or HG2 datasets, and it would be inconsistent to apply uncertainties to some
233 inputs and not others. We discuss the impact of this approach within Section 4.2.
234
235 The published algorithm uncertainties (as stated in the corresponding reference) for each
236 algorithm were propagated through to the algorithm outputs. Following standard propagation
237 methods (Taylor, 1997), *in situ* and algorithm uncertainties were combined assuming that
238 they were uncorrelated (a sum of squares analysis), allowing weighted statistics to be
239 calculated, with each data point weighted by the inverse of the sum of squared uncertainties.
240
241 ***2.3.2 Evaluating output accuracy***
242 Output mean ($\bar{x}_m$), standard deviation (σ_m) and *in situ* carbonate data mean ($\bar{x}_d$) and standard
243 deviation (σ_d) were calculated for each assessment, as well as root-mean-square-difference
244 (RMSD), mean absolute difference (MAD), bias and point-to-point correlation (R) between
245 output and the evaluation (GLODAPv2) *in situ* data. As a check, each of these statistics is
246 presented both weighted and unweighted. Unweighted and weighted RMSD values were
247 usually within about 10%, except in the case of global A_T using the TS13 algorithm, which
248 includes regions with very different algorithm errors. Weighted statistics are used hereafter.
249
250 A potential problem with comparing outputs in this way is that different outputs overlap with
251 different evaluation *in situ* data. Consider the plausible situation in which all outputs perform

252 poorly in coastal waters. All else being equal, an output that is not evaluated using coastal in
253 situ data will produce better statistics than one that is. Therefore, to compare like with like, in
254 each region we considered outputs in pairs, for a given pair calculating RMSD for each of the
255 two outputs using only in situ evaluation matchups shared by both outputs. Each output is
256 given a 'score' of RMSD / $RMSD_{min}$, 1 for the lower RMSD and ≥1 for the other. This is
257 repeated for all possible pairs, then each output is given a 'final score' equal to the mean of
258 all of its scores. To convert this to an estimate of RMSD, we chose a representative output as
259 that with the lowest value of (weighted final score / number of matchups), i.e. the output with
260 the best combination of performance and coverage. The weighted RMSD of this output
261 ($RMSD_{rep}$) was left unchanged and all other output weighted RMSDs in the region were set
262 to $RMSD_{rep}$ × final score / $(\text{final score})_{rep}$, where $(\text{final score})_{rep}$ is the final score of the
263 representative output; this measure is henceforth referred to as RMSDe. Output results can be
264 compared directly within a region, but comparison of output RMSDe between regions or
265 carbonate parameters should be treated with caution. The above calculations could equally be
266 done using MAD in place of RMSD, though we have not done this here.
267
268 ***2.3.2 Evaluating optimal combinations of output elements and importances***
269 To calculate the relative importance of different combinations of output elements (algorithms
270 and/or data inputs) to the output comparison results, we calculated the best RMSDe when a
271 given combination is excluded from all outputs, and divided it by the overall best RMSDe to
272 give an RMSDe ratio. For example, the most effective single exclusion, with an RMSDe ratio
273 of 1.022 (i.e. a 2.2% difference), is A_T using climatological CORA SSS in the Bay of Bengal.
274 The best 13 A_T outputs in the Bay of Bengal all use climatological CORA SSS. Conversely,
275 the best output also uses monthly CCI SST but the second best uses WOA SST, so excluding
276 monthly CCI SST has much less effect. Excluding WOA SST has no effect, since the best

277 output is still the one using monthly CCI SST. Having excluded climatological CORA SSS,
278 the next 14 best A_T outputs all use the TS13 algorithm, so excluding climatological CORA
279 SSS and TS13 has the largest effect among pairs of exclusions in this region. All possible
280 combinations of exclusions were considered, ranked in order of number of elements
281 excluded, then by RMSDe ratio.
282 The resulting comprehensive list is rather hard to read and interpret. To simplify, we created
283 subsets of exclusions objectively considered as most significant. Criteria used were that the
284 RMSDe ratio was greater than 1.01, the exclusions were either all SSS and/or SST inputs or
285 all algorithms, and RMSDe ratio exceeded that of a subset of exclusions by >0.1%. For
286 example, excluding TS13 and SMOS SSS would not qualify, and excluding SMOS and
287 Aquarius SSS would only qualify if its RMSDe ratio were greater than excluding only SMOS
288 and only Aquarius by >0.1%.
289
290 ***2.3.3 Comparing between carbonate parameters***
291 To compare between carbonate parameters in each region, we only considered *in situ*
292 evaluation data points where both A_T and C_T values existed. For each data point and
293 parameter, all outputs producing valid output were considered and the one with the best
294 regional final score was chosen, noting the output-*in situ* difference for this output. The
295 regional RMSD of each parameter was then calculated from the differences at all data points
296 in the region.
297
298 **3. Results**
299 Results are summarized in Figure 1A and B, showing RMSDe for A_T and C_T, Table 4,
300 showing statistics of the lowest-RMSDe output for each SSS source plus HG2 output in each
301 region, and Table 5, showing selected importances. Figures 2 to 4 contain plots of output

versus evaluation (GLODAPv2) *in situ* A_T, C_T and SSS data, with points with depth < 500m and > 300 km from the coast labeled. The supporting data consists of three data collections in separate directories corresponding to all data, minimum depth 500 m, and minimum depth 500 m plus minimum distance to coast 300 km: alternative versions of Figures 1A and 1B for differing masks are shown in Figure S1; matchup data are in Datasets S1 to S5; output statistics are in Datasets S6 to S10; details of output score calculations are in Datasets S11 to S15, and spatial data results (in NetCDF format) are in Datasets S16 to S20. Importances of exclusions are in Datasets S21 (comprehensive) and S22 (selected), and the comparisons between carbonate parameters are in Datasets S23.

Generally there is little to choose between the SSS sources (re-analysed *in situ* or satellite) apart from HG2, which performs less well in all regions, or between monthly and climatological SSS sources. The main differences in performance are between algorithms and between regions, but there is no clearly superior algorithm.

3.1. Total Alkalinity (A_T)

See Table 4 for detailed results. Globally, the best RMSDe values of about 17 μmol kg^{-1} are substantially lower than the SD of the global coverage *in situ* data used for the evaluation (81 μmol kg^{-1}), and in the Amazon and Bay of Bengal they are slightly lower (RMSDe of 55 compared to a SD of 68, and RMSDe of 11 compared to a SD of 16 μmol kg^{-1}, respectively), but in the Greater Caribbean and low-salinity Amazon the RMSDe are higher than the SD, meaning that none of the tested combinations of algorithms and inputs is accurate enough to distinguish natural variations in A_T in these latter two regions.

3.1.1. A_T algorithm and input importances

See Table 5 for details. Globally, S13 performs slightly less well (higher RMSDe) than other algorithms, as do climatological satellite inputs. In the Greater Caribbean, monthly SMOS and Aquarius and climatological Aquarius SSS perform significantly less well. In the Amazon, the Lefevre et al (2010) algorithm and climatological Aquarius and WOA SSS perform less well. In the low-salinity Amazon, monthly SMOS and Aquarius and monthly CCI SST perform best. In the Bay of Bengal, climatological CORA SSS performs best and climatological Aquarius performs significantly less well.

3.1.2. A_T summary

For all case study regions and with respect to these empirical outputs, satellite SSS can reproduce *in situ* measured A_T from the GLODAPv2 evaluation dataset with performance (RMSDe) comparable to, or better than, the re-analysed *in situ* data derived inputs for SSS, and the satellite based A_T is always better than HG2 A_T estimates. Globally HG2 performance is about 85% worse than the best SSS driven outputs, but this reduces to 15-20% in the Amazon plume. Monthly Aquarius and SMOS observations provide a credible solution to monitoring synoptic scale global and regional A_T, though in some challenging regions (Greater Caribbean and low-salinity Amazon plume) none of the tested methods are sufficiently accurate to resolve natural variability.

RMSDe in the Amazon plume is higher than the global RMSDe, reflecting the larger regional standard deviation in the *in situ* data due to the large gradients around the river flow, and RMSDe in the Amazon with SSS < 35 is higher than in the wider Amazon, but the relative performance of SSS inputs is similar.

Excluding the Amazon plume and HG2, the best outputs have bias less than 5 μmol kg^{-1}, or 0.2% of the global mean A_T (of 2450 μmol kg^{-1}) which is similar to the estimated evaluation

dataset *in situ* nominal uncertainty of 0.5% (Bockmon *et al.,* 2015) and the inter-annual variability of A_T observed at oceanic sites such as at the Hawaiian Ocean Time-series station (HOT; ±6 μmol kg^{-1}) (Brix *et al.,* 2004), but lower than the seasonal variability observed at oceanic sites (20 to 30 μmol kg^{-1} at both the Bermuda Atlantic Time-series Study (BATS) (Bates *et al.,* 2012) and the European time series station (ESTOC) (Santana−Casiano *et al.,* 2007). This seasonal variability at BATS and ESTOC is also greater than the best global RMSDe of 17 μmol kg^{-1}. In the Amazon plume, of the monthly SSS sources only SMOS has low bias (2 μmol kg^{-1}), and in the low-salinity Amazon plume, all SSS sources have bias greater than 19 μmol kg^{-1}. These results highlight that these methods (of using satellite observations or re-analysed *in situ* dataset as input to empirical algorithms) can obtain measures of A_T that are not significantly biased relative to the evaluation *in situ* measurements, except in regions of strong spatiotemporal variability. It also shows that these methods are capable of distinguishing the seasonal variability at long-term time series sites, though not the interannual variability at HOT.

3.2. Total Dissolved Inorganic Carbon (C_T)

See Table 4 for detailed results. Globally, the best RMSDe values of 29-30 μmol kg^{-1} are considerably higher than the equivalent global A_T RMSDe values, but still substantially lower than the SD of the global in situ evaluation dataset (69 μmol kg^{-1}), and in the Amazon and Greater Caribbean they are similar (RMSDe 45 compared to SD 53 and RMSDe 19 compared to SD 18 μmol kg^{-1}, respectively), but in the low-salinity Amazon and Bay of Bengal they are higher, meaning that no combination of algorithms and inputs is accurate enough to distinguish natural variations in C_T in these latter two regions.

3.2.1. C_T algorithm and input importances

See Table 5 for details. Globally, L00 and S13g perform better (lower RMSDe) than other algorithms, as do CORA, WOA and monthly SMOS SSS inputs. In the Greater Caribbean, the S13g algorithm performs very poorly and climatological Aquarius SSS performs less well than other SSS inputs. In the Amazon, the S13g algorithm and Aquarius SSS perform less well. In the low-salinity Amazon, the S13g algorithm performs less well, while SMOS, Aquarius and monthly CCI SST perform best. In the Bay of Bengal, the S13 and S13g algorithms perform considerably better than other algorithms and CORA and WOA SSS perform better than other SSS sources.

3.2.2. C_T summary

Similar to A_T, satellite inputs for SSS can reproduce the C_T data (from the GLODAPv2 evaluation dataset) with similar ability, and sometimes better than using re-analysed or climatology *in situ* derived SSS inputs, except for Aquarius in the Amazon plume (Figure 1B), and always better than HG2 C_T estimates. Global HG2 performance is only about 14% worse than the best SSS driven outputs, but this increases to over 80% in the Bay of Bengal and Greater Caribbean. As with A_T, monthly SMOS and Aquarius observations provide a credible solution to monitoring synoptic scale global and in some cases regional C_T. Best RMSDe values are higher for C_T than A_T globally and in the Greater Caribbean and Bay of Bengal, but lower in both Amazon plume regions. Again, in some challenging regions (low-salinity Amazon plume and Bay of Bengal), none of the tested methods are sufficiently accurate to reproduce natural variations.

Bias in the C_T outputs is generally greater and more variable than that in the A_T outputs, except in the Amazon plume where non-HG2 monthly and climatological bias is uniformly less than 3 μmol kg^{-1}. The smallest bias among the best global monthly outputs is monthly

CORA with -9 µmol kg^{-1}, in the Greater Caribbean monthly SMOS and Aquarius have bias of 3 and 4 µmol kg^{-1} respectively, monthly outputs in the low-salinity Amazon are all strongly biased, the smallest being CORA with 45 µmol kg^{-1}, and in the Bay of Bengal monthly CORA has bias of 16 µmol kg^{-1} while climatological datasets (WOA, CORA, SMOS) have lower bias (-11, -12, -14 µmol kg^{-1} respectively). For comparison, the *in situ* nominal uncertainty of 0.5% (Bockmon *et al.,* 2015) at the global average C_T of 1900 µmol kg^{-1} would be 9.5 µmol kg^{-1}, the inter-annual variability of nC_T is ±4 µmol kg^{-1} at HOT and ±8 µmol kg^{-1} at ESTOC (Brix *et al.,* 2004, Santana−Casiano *et al.,* 2007), while the seasonal amplitude of nC_T at HOT is 15 µmol kg^{-1} (Brix *et al.,* 2004) and those of C_T at ESTOC and BATS are 20-30 and 40-50 µmol kg^{-1}, respectively (Santana−Casiano *et al.,* 2007, Bates *et al.,* 2012). The biases in these outputs are also comparable to the systematic biases found by Lee *et al.* (2000) when comparing algorithm derived nC_T to nC_T calculated from A_T and pCO_2 data (-3 to +15 µmol kg^{-1}). Thus, these results highlight that some of the outputs evaluated can obtain measures of C_T that are not significantly biased relative to the *in situ* evaluation measurements, though overall uncertainties may be high relative to the variability at these long-term monitoring sites.

3.3. A_T and C_T Algorithm biases

In the Amazon Plume, the best output was strongly correlated with the evaluation *in situ* A_T or C_T, but with a slope significantly different from 1 (Figures 2B and 3B). Replacing monthly satellite SSS with monthly or climatological CORA SSS (re-analysed and interpolated *in situ*) produces similar biases (Figure 4), suggesting that the cause of the bias is not specific to satellite SSS or monthly data.

A possible explanation of this bias would be that the algorithm is not capturing the two endmember mixing from the river with zero salinity and some finite, but significant A_T and C_T. However, the regional algorithms for the Amazon plume implicitly include the river endmember, as they are based on measurements that include low and high salinity values, and each published algorithm finds a strongly linear relationship between salinity and A_T or C_T. Since the bias using these algorithms is similar to that using the global algorithms, we can conclude that the endmember issue is not the main reason for the bias.

Another possible explanation of the bias would be sampling of water with low SSS, A_T and C_T in regions with high spatial and temporal SSS variability, as found in the Amazon plume and particularly within the low salinity Amazon plume region. Satellite and CORA data represent an average over at best one grid cell (about 10^4 square kilometers at the equator) and one month (or the same month in a range of years in the case of climatological data), while an *in situ* measurement samples a very small volume of water and is almost instantaneous. The effect of this averaging is to remove variability that occurs on smaller spatial and temporal scales. For example, low *in situ* salinity in the Amazon plume may be caused by small eddies or filaments of river water not resolvable at the grid cell scale, or by interannual variations in the plume extent. In this situation, extreme evaluation *in situ* values will consistently be matched with outputs driven by satellite and CORA data that are closer to the large-scale and long-term mean. If the salinity distribution is strongly one-tailed, as in the Amazon plume, and the cause of anomalies is consistently unresolved by the averaged data, the *in situ* evaluation data will consistently give lower salinity than the averaged data, as observed here (Figure 5). This issue is likely to be one cause of the large biases evident in all output results (re-analysed *in situ* and satellite input derived) for the low salinity Amazon region.

449

450 A third possible explanation for the bias arises from fundamental differences between the *in*
451 *situ* measurements used to calibrate the original algorithms and the satellite salinity
452 observations used herein as input to the algorithms. Satellite SSS observations represent the
453 conditions in the top 10 mm of the water (Boutin *et al.,* 2013), whereas *in situ* SSS
454 observations are typically sampled from ≥1 m below the surface. This can result in
455 geophysical sources of variation between satellite and *in situ* salinity, which are linked to
456 vertical salinity stratification, and these features are prevalent in regions of rain, oceanic
457 fronts and river outflow (Boutin *et al.,* 2013; Boutin *et al.,* 2016;Drucker *et al.,* 2014). For
458 example, salinity gradients created by freshwater plumes can complicate the comparison of
459 satellite and *in situ* salinity measurements; a difference of 2–5 pss m^{-1} has been observed
460 across the halocline in the Amazon plume (Lentz *et al.,* 1995). Plumes can also cause
461 horizontal salinity gradients with spatial scales smaller than the footprint of the satellite
462 radiometers. Typical horizontal SSS gradients for the plumes from the Amazon (Lentz *et al.,*
463 1995) or Congo (Chao *et al.,* 2015) exceed 0.2 pss km^{-1} and extend more than 250 km from
464 the river mouth. Therefore, in the vicinity of a river plume, a spatially sparse array of *in situ*
465 sensors can exhibit very different SSS variability from that observed by a satellite sensor,
466 even if the measurements are all coincident. Similarly, high-frequency SSS variations (e.g.
467 tidal effects) can be undersampled by satellite-derived SSS products due to the relatively long
468 revisit time of the satellite (2–3 days for SMOS and 7 days for Aquarius). Accounting for the
469 depth-related differences should increase the accuracy of the outputs, and a rigorous
470 treatment might adapt the theory currently used to reconcile *in situ* and satellite SST
471 (Merchant *et al.,* 2014). We therefore recommend that the satellite SSS community consider
472 investigating this theory for SSS.
473

In the absence of a rigorously tested explanation for these biases, and to demonstrate the potential gain from reducing them, we simply note that linear regression of the best output against the evaluation *in situ* A_T and C_T reduces the RMSD (actual, not estimated) in the low salinity Amazon plume region from 215 to 48 μmol kg^{-1} (a 77% reduction) for A_T and from 67 to 50 μmol kg^{-1} (26%) for C_T.

3.4. Comparison of A_T with C_T

Results are shown in Dataset S23, showing that in direct comparisons at each matchup position, the A_T outputs have a 42% lower RMSDe than C_T globally, 41% lower in the Bay of Bengal and 21% lower in the Caribbean, indicating that A_T outputs can generally be retrieved more successfully than C_T outputs. However, A_T has a 13% higher RMSDe than C_T in the Amazon and 9% higher in the low salinity Amazon using the same algorithms as in the global case, so this relationship is not universal.

3.5. Multi-year synoptic observations

The methods evaluated here enable the first multi-year synoptic scale observations of A_T and C_T spatial mixing and distributions. To demonstrate their application we characterise the synoptic scale, extent and influence of river-flow-dominated alkalinity mixing in the Amazon plume and western North Atlantic. The Amazon Plume exhibits a two-end-member alkalinity-salinity mixing regime, resulting in a strong linear relationship between alkalinity and salinity (Cai *et al.,* 2010), and mixing between river water and seawater is the dominant controlling factor of the alkalinity-salinity relationship in the western North Atlantic (Jiang *et al.,* 2014). The accuracy assessment means that we can illustrate SMOS or Aquarius observational-based C_T and A_T monitoring of the Amazon plume along with a calculated estimate of the combined uncertainty in C_T and A_T (provided by the RSMDe and bias).

To simplify the interpretation we present results using the same algorithm for monthly SMOS and Aquarius, so that any differences are due solely to the SSS source. For A_T, the best output with both SMOS and Aquarius is TS13 with WOA nitrate, with RMSDe of 57.7 μmol kg^{-1} for SMOS and 58.4 μmol kg^{-1} for Aquarius. For Ct the best Aquarius outputs use different algorithms to the best SMOS outputs, and perform less well. Therefore for simplicity we present results of using SMOS and Aquarius with a single algorithm and input pairing (L00 and climatological CORA SST), with RMSDe of 45.0 μmol kg^{-1} for SMOS and 52.2 μmol kg^{-1} for Aquarius. We calculated A_T and C_T time series for the Amazon plume using the above algorithm and input pairings, producing monthly Aquarius and SMOS derived A_T and C_T collectively covering the time period 2010 to 2016.

Figure 6 shows the regional (0-15°N, 45-62°W) mean SMOS and Aquarius SSS, climatological CORA SST, output A_T and output C_T, in relation to climatological Amazon discharge data from the Obidos gauge located 750 km from the ocean (Perry *et al.,* 1996). The discharge data are only provided as an indication of variations in Amazon discharge and will not represent the total flow (Salisbury *et al.,* 2011). In a given month with both SMOS and Aquarius data, we calculate mean SSS using only cells in which both have valid data, in order to compare like with like. If this is not done, and one dataset extends into a low salinity region not covered by the other, large spurious differences can occur, e.g. in May 2014 inconsistent masking causes the regional mean Aquarius SSS to be 1.24 units lower than SMOS SSS (results not shown), a difference that reduced to 0.07 units with consistent masking. Maximum SSS consistently occurs during December and January and minimum SSS occurs during May-July, 1-3 months after the maximum discharge in April, both of which are consistent with previous findings (Salisbury *et al.,* 2011). As expected, A_T and C_T

maxima occur in phase with the variations in SSS, and typically lag the peaks in SST by one to two months, with regional A_T each year varying between 2230 and 2370 μmol kg^{-1} and C_T varying between 1890 and 2000 μmol kg^{-1}.

Figure 7 reveals the seasonal patterns in A_T over the same period as shown in Figure 6B in relation to the dynamics of the Amazon discharge and their interaction offshore with the along-shore North Brazilian Current, North Equatorial Counter Current and Guyana Current. The August 2011 SSS conditions are shown in Figure 7A. Clear annual cycles and river plume features are apparent in the observed A_T, with the Amazon plume influencing A_T more than 1000 km offshore of the mouth of the Amazon (Figure 7B-D). During June-July each year, very low A_T values reaching below 2100 μmol kg^{-1} are apparent at the mouth of the Amazon (Figure 7D), the timing of which is consistent with the observed annual minima in SSS (Salisbury *et al.,* 2011) (see also Figure 6). Further west the river plume spreads out as it interacts with the along-shore currents, resulting in A_T in the region of ~2150 μmol kg^{-1} up to ~1700 km offshore (regions of yellow up to ~17°N in Fig. 3C). The Amazon plume has been observed to bifurcate during the northern hemisphere summer months (Del Vecchio *et al.,* 2004), with one part of the river plume heading north-west and a second jet retroflected to the east (Salisbury *et al.,* 2011). This bifurcation is apparent each year around August (Figure 7A-D), with an isolated feature of A_T around 2000-2100 μmol kg^{-1} appearing 500-1000 km offshore and to the east of the river mouth, although this feature was less pronounced during 2014 (regions of yellow between 5-10°N in Figure 7D).

Figure 8 shows Aquarius and SMOS monthly A_T for April 2012 overlaid with 100 *in situ* A_T observations from the GLODAPv2 dataset (Olsen *et al.,* 2016) collected at 3 m nominal depth during 13 consecutive days in April and May 2012, and Figure 9 shows the equivalent

549 plot for C_T. Despite the different temporal resolutions, the change in magnitude of the
550 observations (the gradient) between the open ocean data and those close to, and within the
551 river plume, are generally comparable to the synoptic scale observations. The high monthly
552 temporal variations along the ~52°W latitudinal transect are illustrated in Figure 7D. The
553 differences between *in situ* and synoptic scale observations are discussed in section 3.3. This
554 comparison highlights the power of the synoptic scale observations, allowing the *in situ*
555 observations to be placed within their wider spatial and temporal context. It also highlights
556 how the synoptic observations characterise the distributions and mixing at the very surface of
557 the water column and how these can be different from that observed *in situ* (at a nominal
558 depth of 3 m), particularly in regions of strong river plume influence. Figures 8 and 9 could
559 suggest that lower values of A_T and C_T are found below the surface in the coastal region,
560 whereas offshore the salinity, A_T and C_T are vertically well mixed. A combination of *in situ*
561 and synoptic scale observations could be used to understand the near-surface vertical profile
562 of A_T.
563
564 **4.0 Discussion**
565 **4.1 Bay of Bengal**
566 Because there are permanent and strong radio-frequency interference sources around the
567 coasts of Asia, SSS measurements from SMOS and Aquarius are likely to be of a lower
568 quality in the Bay of Bengal. However, the paucity of *in situ* measurements in the Bay of
569 Bengal in the satellite salinity era makes comparison difficult. The Bay of Bengal *in situ* A_T
570 data measured in 2014 were not included in the main analysis due to their proximity to the
571 coast (and so were removed due to the masking), and their inclusion causes the RMSDe of
572 HG2 to increase to over 600 μmol kg^{-1} (Figure S1). This demonstrates the importance of
573 comparing like with like when evaluating the outputs and also highlights the influence of

574 focusing on evaluation data without terrigenous influence. The low number of *in situ* data
575 points used in the Bay of Bengal accuracy assessment highlights that the evaluation of output
576 datasets (from both satellites and re-analysed *in situ*) will be biased against small-scale
577 variability that may be captured by the *in situ* observation data used for the evaluation,
578 particularly when *in situ* validation sites are relatively near-shore and the effect of riverine
579 water flow is more pronounced. This was the case for the 2014 *in situ* dataset that was
580 omitted from the main accuracy assessment due to falling within the masked area: the site
581 was part of the Sundarbans Biological Observatory Time Series, representing the coastal part
582 of the Sundarbans mangrove ecoregion, which can act as a source and a sink of CO_2 during
583 pre-monsoon (April-May) (Akhand *et al.,* 2017), and it is also an area that receives high
584 freshwater discharge (~42000 m^3 s^{-1}) along with local heavy seasonal precipitation, in
585 addition to increasing anthropogenic pressure (Choudhury *et al.,* 2015). The other case study
586 regions have more data available for comparison and therefore this variability may be
587 averaged out in the *in situ* data binning process. It is essential that more *in situ* carbonate
588 system data are collected to elucidate these issues for this complex region (the Bay of
589 Bengal), which has a strong riverine influence, and to characterize the variability on a wider
590 scale than has currently been observed (Sarma *et al.,* 2012; Samanta *et al.,* 2015).
591
592 A large area of the Bay of Bengal is characterized by pCO_2 levels far below the atmospheric
593 value (i.e. a large gradient between atmospheric and oceanic pCO_2), which is more prominent
594 during the north-east monsoon when the air-sea pCO_2 gradient exceeds 100 µatm (Akhand *et*
595 *al.,* 2013; Ganguly *et al.,* 2011). The enhanced gradient is possibly due to new biological
596 production sustained by excessive nutrient inputs from the Ganga-Brahmaputra-Meghna river
597 basins, thus influencing the carbonate system via net organic production. Additionally, the
598 presence of non-carbonate alkalinity in these regions (e.g. riverine contributions of organic

599 species including humic acid) can result in A_T that is not correlated with salinity (Akhand *et*
600 *al.,* 2013). Only 14 of the outputs overlapped in space and time with the 2014 *in situ* data that
601 captured this very near-shore variability, resulting in the apparent poor performance of these
602 14 outputs before coastal masking. If the other outputs had also captured this near-shore
603 variability they may also have had reduced performance. Low satellite SSS coverage due to
604 the issues of radio-frequency interference described above will have also contributed to lower
605 performance of the satellite data driven outputs in this region. Improvements in satellite data
606 coverage in coastal regions together with increased *in situ* data are likely to begin resolving
607 these issues.
608
609 **4.2 The need for continued efforts in quantifying uncertainties**
610 The problem of uncertainties, and their propagation through the analysis, is an ongoing one.
611 Here, the estimated uncertainties in the *in situ* measurements used for the evaluation and
612 algorithm uncertainties were included in the analysis where they were quantifiable (i.e.
613 nominal uncertainties for the C_T and A_T *in situ* evaluation measurements and the propagation
614 of the empirical algorithm uncertainties). Published remote sensing uncertainties are
615 available, however no such information exists for the other input datasets; and even within
616 the carbonate system there are still many challenges to fully defining *in situ* and laboratory
617 measurement uncertainties (Andrew Dickson, pers. comms.; Bockmon and Dickson, 2015).
618 Therefore, quantification of associated uncertainties for all of the input data sources requires
619 continued work. Furthermore, unavoidably in this analysis, data used to evaluate the
620 algorithm outputs were unlikely to be wholly independent from the data used to create the
621 algorithms. In order to have a fully independent evaluation dataset, original datasets would be
622 required to develop the algorithms whilst keeping enough data separate from the algorithm
623 development process to enable an independent evaluation. This was not possible in this initial

assessment due to the general dearth of measurements in some regions, and due to ambiguity over which measurements were used to develop the historical algorithms.

However in relation to our calculated combined uncertainties of our outputs, the estimated combined uncertainties from Fine *et al.* (2017) of smaller than ±20 μmol kg^{-1} for retrieving global A_T using satellite salinity and SST are consistent with our global results of RMSDe of 17 μmol kg^{-1}, bias < 5 μmol kg^{-1}. This gives further confidence in the approach taken here. We note however that Fine *et al.* (2017) misinterpreted the uncertainty information provided by Olsen et al., (2016), as Olsen *et al.* only state the bias, which as previously discussed is only one component of a Type A uncertainty.

To test the sensitivity of the output uncertainties to the SST and SSS satellite remote sensing input data uncertainties, the latter were propagated through the analysis for all global empirical A_T algorithms (TS13, Lee06, Lee00, S13, S13g) for two example months (January and July). This results in A_T output uncertainties (due solely to satellite SSS and SST input data) of 0.2 to 0.8% (Table 6), which is close to the nominal *in situ* uncertainties of 0.5%, or ±10 umol kg^{-1}. The combined uncertainty in most of the studied regions is considerably greater than this, implying that (in the global case at least) the other components of the uncertainty budget dominate over the remote sensing input data uncertainty.

4.3 The need for algorithm retraining and the collection of *in situ* observations

Only seven global and five regional algorithms were presented here, in addition to output of A_T and C_T from HG2, primarily because these were the only algorithms from the published literature that did not require additional re-parameterization for all the case study regions. Future efforts are needed to perform this re-fitting, not only for additional A_T and C_T

649 algorithms, but also for the remaining carbonate system parameters (pCO_2 and pH). This is a
650 demanding task; with just the 14 algorithms and model outputs used here, 1070 outputs were
651 compared in the round-robin comparisons. Further, where few *in situ* measurements of a
652 carbonate variable exist (e.g. pH), information could be obtained for future assessments by
653 calculating this variable from two of the other carbonate variables (e.g. C_T and A_T) along with
654 temperature and salinity. Calculating the variable in this way does introduce additional
655 uncertainties, thus to be truly beneficial, such outputs should include the propagation of all
656 uncertainties. A future assessment of the exploitation of satellite SSS will require further
657 analysis of temporally resolved (rather than climatological) satellite observations, using new
658 *in situ* data. We found only three cruises within GLODAPv2 that overlap with satellite
659 salinity observations in our regions: none in the Bay of Bengal, one in the Amazon plume at
660 the beginning of May 2010 (the first month of reliable SMOS data after its launch in
661 November 2009) and two in the Amazon plume in April and May 2012 (shown in Figures 8
662 and 9), one of which overlapped with the Greater Caribbean (only 6% and 3% of the
663 GLODAPv2 data correspond to SMOS and Aquarius eras respectively). Hence coverage
664 where we have both *in situ* and satellite observations is very limited spatially, seasonally and
665 interannually, highlighting the need for further *in situ* data. It should also be noted that the
666 lowest uncertainties achieved using these satellite observation-based and empirical
667 approaches are still greater than the nominal *in situ* and laboratory measurement uncertainties
668 (of ±10 μmol kg^{-1}) so the methods presented here are unlikely to ever be a substitute for *in*
669 *situ* measurements. Their strength is in providing synoptic data to fill the inevitable gaps in
670 the *in situ* data coverage. To enable all new *in situ* data to be fully exploited by the Earth
671 observation community they need to have been collected following international protocols (as
672 defined by Dickson et al., 2007), analysed using traceable standards (as advocated by
673 Bockmon and Dickson, 2015) enabling the provision of a complete uncertainty budget

(quantified as a Type A uncertainty, BIPM, 2008). If possible, the historical data contained within the GLODAPv2 dataset would benefit from the inclusion of some indication of their uncertainty budget e.g. a simple 'high', 'low' or 'unknown' determined using existing metadata and/or expert interpretation and opinion via a Type B uncertainty approach as defined by BIPM, (2008). Similarly, the CORA re-analysis and WOA climatology data would benefit from similar additions as these datasets lack any uncertainty information.

4.4 Earth system model performance

It should be noted that we would not expect a free running global Earth system model such as HG2 to perform well regionally, though the poor global A_T performance and the relatively good performance in the Amazon plume were surprising. We include HG2 in the comparison mainly to illustrate how this methodology could be used to compare model data with quite different input sources such as satellite data. Our results provide a potentially useful dataset (including uncertainty information) to evaluate and challenge Earth system model outputs.

5. Conclusions

We demonstrate that satellite SSS and SST data are, in conjunction with empirical algorithms, able to successfully reproduce both A_T and C_T in four regions (globally, the Caribbean, the Amazon and the low salinity Amazon) as well as or better than *in situ*-derived (re-analysed) SSS and SST using the same empirical algorithms, or a global Earth system model dataset, with the advantage that satellite datasets are acquired daily, on average, with synoptic coverage.

The ability to derive key surface carbonate system parameters from satellite observed SSS and SST offers the potential for quantifying natural variability, as well as monitoring the present state of these important parameters through space and time. Satellite sensors provide

699 a significant advantage over traditional *in situ* derived climatologies because of the ability to
700 provide synoptic and frequent observations of global oceans. Critically, many of the satellites
701 that provide these data are already in operation, hence historic satellite sensor datasets could
702 be used with these algorithms to elucidate changes over longer periods of time. These
703 satellite methods should not replace ongoing *in situ* measurements, but should complement
704 and enhance them by providing observations in periods where there are gaps in both time and
705 space. Ongoing *in situ* data are essential to improve our ability to exploit satellite data, for
706 example through enhanced parameterization of the algorithms. Satellites are also only able to
707 measure surface waters, and are unable to measure under ice. These gaps must be filled with
708 *in situ* data. Similarly, the evolving nature of the carbonate system due to anthropogenic
709 forcing means that it is likely that these empirical algorithms will need to be periodically re-
710 trained to maintain their performance. Hence the algorithms and methods utilized are useful
711 for studying seasonal and inter-annual variations and episodic events, but may not be suitable
712 for resolving longer-term trends.
713
714 The assessment presented here, which represents a significant effort and extensive analysis,
715 provides the baseline performance against which any future algorithm re-training or re-
716 calibration attempts can be compared.
717
718 **Acknowledgments**
719 This work was funded by the European Space Agency (ESA) Support to Science Element
720 (STSE) Pathfinders Ocean Acidification project (contract No. 4000110778/14/I-BG,
721 http://www.pathfinders-oceanacidification.org/) with additional support from the ESA
722 Satellite Oceanographic Datasets for Acidification, OceanSODA, (contract No.
723 4000112091/14/I-LG, https://www.esa-oceansoda.org/). The authors thank Professor Andrew

724 Dickson, Scripps Institution of Oceanography, for discussions about carbonate chemistry
725 uncertainties and error propagation.
726
727 **Tables**
728 Table 1: Summary of algorithms, their dependencies and the region for which they were
729 originally developed. A_T = Total Alkalinity, C_T = Dissolved Inorganic Carbon; SSS = Sea
730 Surface Salinity, SST = Sea Surface Temperature, DO = Dissolved Oxygen, N = nitrate, Si =
731 silicate, P = phosphate.

Product	Name	Dependencies	Reference	Region
A_T	TS13	SSS, N	(Takahashi and Sutherland 2013)	Global
A_T	L06	SSS, SST	(Lee et al. 2006)	Global
A_T	S13	SSS, SST, DO, Si, P	(Sasse et al., 2013)	Global
A_T	S13g	SST, SSS, DO, Si, P	(Sasse et al., 2013)	Global
A_T		SSS	(Lefèvre et al. 2010)	APR
A_T		SSS	(Cai et al. 2010)	GCR, APR
C_T	L00	SSS, SST, N	(Lee et al. 2000)	Global
C_T	S13	SST, SSS, DO, N, Si, P	(Sasse et al., 2013)	Global
C_T	S13g	SST, SSS, DO, N, Si, P	(Sasse et al., 2013)	Global
C_T		SSS	(Lefèvre et al. 2010)	APR
C_T		SSS	(Bonou et al. 2016)	APR

732
733
734
735 Table 2: Datasets used as inputs to the empirical algorithms. SSS = sea surface salinity, SST
736 = sea surface temperature, DO = dissolved oxygen.

	Type	Name	Time period	References
SSS	Satellite	SMOS (CATDS v2)	2010 - 2014	(Reul and Team 2011)
SSS	Satellite	Aquarius	2011 - 2014	(Le Vine et al. 2014)
SST	Satellite	ESA SST CCI	1992 - 2010	(Merchant et al. 2012)
SSS, SST	Re-analysis	CORA v4.0	1990 - 2012	(Cabanes et al. 2013)
SSS, SST, DO, N, P, Si	Climatology	WOA	1970 - 2012	(Garcia et al. 2014a; Garcia et al. 2014b; Locarnini et al. 2013; Zweng et al. 2013)

737

738

739 Table 3: *In situ* carbonate chemistry datasets used for evaluating the outputs. All datasets for
740 each variable were combined into one dataset that was averaged monthly on a 1°x1° grid.
741 The Bhadury et al. coastal data are from a sampling station located on the coast of India at
742 21° 40' 40.6" N, 88° 9' 19.2"E, shown in Figure 1 of Choudhury et al. (2015) (Station 3).
743 The Findlay et al. research cruise data are from cruises off the Svalbard and Greenland
744 coasts, 78° 53'-59' N, 11° 42'-12° 27' E and 70° 14-49' N, 22° 4-32'W respectively.

	Dataset name	Time period	References
A_T, C_T	GLODAPv2	1970 – 2013	(Olsen et al. 2016)
A_T, C_T	OWS Mike	2001 - 2007	(Findlay et al. 2008)
A_T	Bhadury et al. coastal data	2014	(Choudhury et al. 2015)
A_T, C_T	Findlay et al. research cruise	2012 – 2014	[Findlay *pers. comm.*]

745

746

747 Table 4: Coverage, RMSDe and bias of the lowest RMSDe output for each SSS source in
748 each region and carbonate parameter. Note that coverage is compared to all possible
749 matchups, so recent SSS sources such as satellites have relatively low coverage.

SSS INPUT	**COVERAGE (%)**	**RMSDe (µmol kg^{-1})**	**BIAS (µmol kg^{-1})**
GLOBAL A_T (N=6019)			
***In situ* SD for comparison**		**81**	
SSS_CORA	88	17	0

SSS_AQUARIUS	4	17	3
SSS_SMOS	6	17	-5
HG2	100	32	-17
SSS_CORA_CLIM	96	17	-2
SSS_WOA_CLIM	96	17	0
SSS_SMOS_CLIM	94	18	1
SSS_AQUARIUS_CLIM	93	18	-5
HG2_CLIM	100	31	-16
G CARIB A_T (N=55)			
***In situ* SD for comparison**		**13**	
SSS_CORA	96	17	3
SSS_AQUARIUS	13	19	-4
SSS_SMOS	13	20	-4
HG2	100	50	50
SSS_CORA_CLIM	100	17	-4
SSS_WOA_CLIM	100	17	3
SSS_SMOS_CLIM	100	17	3
SSS_AQUARIUS_CLIM	100	19	2
HG2_CLIM	100	48	50
AMAZON A_T (N=108)			
***In situ* SD for comparison**		**68**	
SSS_SMOS	31	58	1
SSS_AQUARIUS	12	58	17
SSS_CORA	78	59	10
HG2	100	75	43
SSS_CORA_CLIM	100	57	-1
SSS_SMOS_CLIM	100	59	-2
SSS_AQUARIUS_CLIM	100	60	1
SSS_WOA_CLIM	100	60	-6
HG2_CLIM	100	73	41
AMAZON S<35 A_T (N=15)			
***In situ* SD for comparison**		**115**	
SSS_SMOS	20	132	124
SSS_CORA	20	132	125
SSS_AQUARIUS	87	132	26
HG2	100	172	128
SSS_CORA_CLIM	100	132	25
SSS_AQUARIUS_CLIM	100	133	-19
SSS_WOA_CLIM	100	135	24
SSS_SMOS_CLIM	100	136	20
HG2_CLIM	100	166	121
BENGAL A_T (N=23)			
***In situ* SD for comparison**		**16**	
SSS_CORA	96	11	-3
HG2	100	52	77
SSS_CORA_CLIM	100	10	-3
SSS_SMOS_CLIM	100	10	3
SSS_WOA_CLIM	100	11	5
SSS_AQUARIUS_CLIM	100	11	-2
HG2_CLIM	100	55	83
GLOBAL C_T (N=6689)			
***In situ* SD for comparison**		**69**	

SSS_CORA	90	30	-9
SSS_SMOS	6	30	-13
SSS_AQUARIUS	3	30	23
HG2	100	33	-13
SSS_WOA_CLIM	99	29	-8
SSS_CORA_CLIM	99	29	-8
SSS_AQUARIUS_CLIM	96	30	21
SSS_SMOS_CLIM	97	31	22
HG2_CLIM	100	34	-17
G CARIB C_T (N=53)			
***In situ* SD for comparison**		**18**	
SSS_CORA	96	19	14
SSS_SMOS	13	19	3
SSS_AQUARIUS	13	19	4
HG2	100	42	52
SSS_WOA_CLIM	100	19	9
SSS_CORA_CLIM	100	19	10
SSS_SMOS_CLIM	100	19	10
SSS_AQUARIUS_CLIM	100	19	8
HG2_CLIM	100	36	45
AMAZON C_T (N=155)			
***In situ* SD for comparison**		**53**	
SSS_CORA	85	45	3
SSS_SMOS	21	45	3
SSS_AQUARIUS	8	48	0
HG2	100	57	33
SSS_CORA_CLIM	100	45	0
SSS_SMOS_CLIM	100	45	0
SSS_WOA_CLIM	100	45	-2
SSS_AQUARIUS_CLIM	100	46	-1
HG2_CLIM	100	53	30
AMAZON S<35 C_T (N=17)			
***In situ* SD for comparison**		**96**	
SSS_SMOS	18	109	100
SSS_AQUARIUS	18	109	108
SSS_CORA	94	109	45
HG2	100	132	118
SSS_SMOS_CLIM	100	109	3
SSS_CORA_CLIM	100	109	44
SSS_AQUARIUS_CLIM	100	111	21
SSS_WOA_CLIM	100	111	45
HG2_CLIM	100	125	108
BENGAL C_T (N=24)			
***In situ* SD for comparison**		**10**	
SSS_CORA	96	19	16
HG2	100	36	51
SSS_CORA_CLIM	100	18	-12
SSS_WOA_CLIM	100	18	-11
SSS_SMOS_CLIM	100	19	-14
SSS_AQUARIUS_CLIM	100	20	-17
HG2_CLIM	100	34	48

750

751 Table 5: Selected importances of exclusions for each carbonate parameter and region. A
752 source of SSS or SST can be monthly (M), climatological (C) or all (no prefix). Importances
753 are the percentage increase in RMSDe as a result of excluding all the listed inputs or
754 algorithms. Only exclusions mentioned in the text are listed here, more complete lists can be
755 found in Supplementary Datasets S21 (comprehensive) and S22 (selected).

EXCLUSIONS	IMPORTANCE (%)	NOTES
(GLOBAL A_T)		
TS13,L06,S13g	3.1	Only leaves S13,HG2
TS13,L06,S13g,S13	85	Only leaves HG2
CORA,M SMOS,M Aquarius,WOA SSS	3.0	Only leaves C SMOS,C Aquarius
CORA,SMOS,M Aquarius,WOA SSS	4.1	Only leaves C Aquarius
(G CARIB A_T)		
CORA,WOA,C SMOS SSS	13	Only leaves M SMOS,Aquarius
TS13,L06,S13g,Cai10	2.9	Only leaves S13,HG2
TS13,L06,S13g,Cai10,S13	286	Only leaves HG2
CORA,WOA,C Aquarius,C SMOS SSS	16	Only leaves M SMOS,M Aquarius
CORA,WOA,Aquarius,C SMOS SSS	18	Only leaves M SMOS
(AMAZON A_T)		
TS13,L06,S13,S13g	2.6	
TS13,L06,S13,S13g,Cai10	4.4	Only leaves Lefevre10,HG2
SMOS,CORA,M Aquarius SSS	4.0	Only leaves C Aquarius,WOA SSS
TS13,L06,S13,S13g,Cai10,Lefevre10	26	Only leaves HG2
SMOS,CORA,Aquarius SSS	5.1	Only leaves WOA SSS
(AMAZON S<35 A_T)		
M SMOS,M Aquarius SSS,M CCI SST	2.5	All monthly satellite data
M SMOS,Aquarius SSS,M CCI SST	3.2	
SMOS,Aquarius SSS,M CCI SST	4.6	
M SMOS,Aquarius,CORA SSS	2.9	
TS13,L06,S13,S13g,Cai10,Lefevre10	26	Only leaves HG2
(BENGAL A_T)		
C CORA SSS	2.2	
C CORA,C SMOS SSS	5.1	
C CORA,C SMOS,WOA SSS	6.4	Only leaves M CORA,C Aquarius
TS13,L06,S13	3.7	Only leaves S13g,HG2
TS13,L06,S13,S13g	517	Only leaves HG2
CORA,C SMOS,WOA SSS	8.1	Only leaves C Aquarius
(GLOBAL C_T)		
L00	3.6	
L00,S13g	5.3	
L00,S13g,S13	14	Only leaves HG2
CORA,WOA,M SMOS SSS	3.6	
CORA,WOA,M SMOS,M Aquarius SSS	4.4	Only leaves C SMOS,C Aquarius
CORA,WOA,Aquarius,M SMOS SSS	7.7	Only leaves C SMOS
(G CARIB C_T)		
L00,S13	73	Only leaves S13g and HG2
L00,S13,S13g	90	Only leaves HG2
SMOS,CORA,WOA,M Aquarius SSS	3.9	Only leaves C Aquarius
(AMAZON C_T)		
L00,S13,Bonou16,Lefevre10	2.1	Only leaves S13g and HG2

L00,S13,Bonou16,Lefevre10,S13g	19	Only leaves HG2
SMOS,CORA,WOA SSS	3.6	Only leaves Aquarius
SMOS,CORA,C Aquarius,WOA SSS	7.0	Only leaves M Aquarius
(AMAZON S<35 C_T)		
L00,S13,Bonou16,Lefevre10	2.2	Only leaves S13g and HG2
L00,S13,Bonou16,Lefevre10,S13g	15	Only leaves HG2
SMOS,Aquarius SSS,M CCI SST	2.6	Only leaves CORA,WOA SSS
SMOS,Aquarius,CORA SSS,M CCI SST	4.9	Only leaves WOA SSS
(BENGAL C_T)		
S13	2.1	
S13,S13g	9.9	
C CORA,WOA SSS	2.1	
L00,S13,S13g	83	Only leaves HG2
CORA,WOA SSS	3.6	
CORA,C SMOS,WOA SSS	5.9	

Table 6: Testing the sensitivity of the output uncertainties to that of the satellite remote sensing input data uncertainties using all global A_T algorithms (TS13, Lee06, Lee00, S13 and S13g) and exemplar uncertainties from the literature (for SST, Merchant *et al.,* (2014) gives ±0.15°C; for SSS, Boutin *et al.,* (2018) gives ±0.2). The output uncertainties are given as a percentage of a global value of 2000 μmol kg^{-1} and the quoted values are the maximum open-ocean values calculated for all data within latitudes <±60°.

Algorithm	**Uncertainty in A_T due to SSS (%)**	**Uncertainty in A_T due to SST (%)**
TS13	**<±0.8**	**N/A**
Lee06	**<±0.7**	**<±0.2**
Lee00	**<±0.9**	**<±0.2**
S13	**<±0.6**	**<±0.1**
S13g	**<±0.6**	**<±0.1**

764 **Figures**

(A)

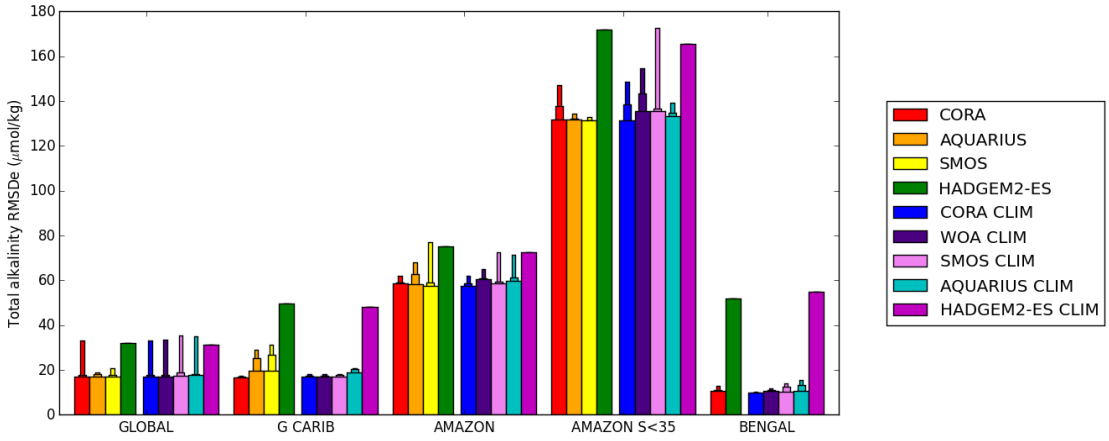

(B)

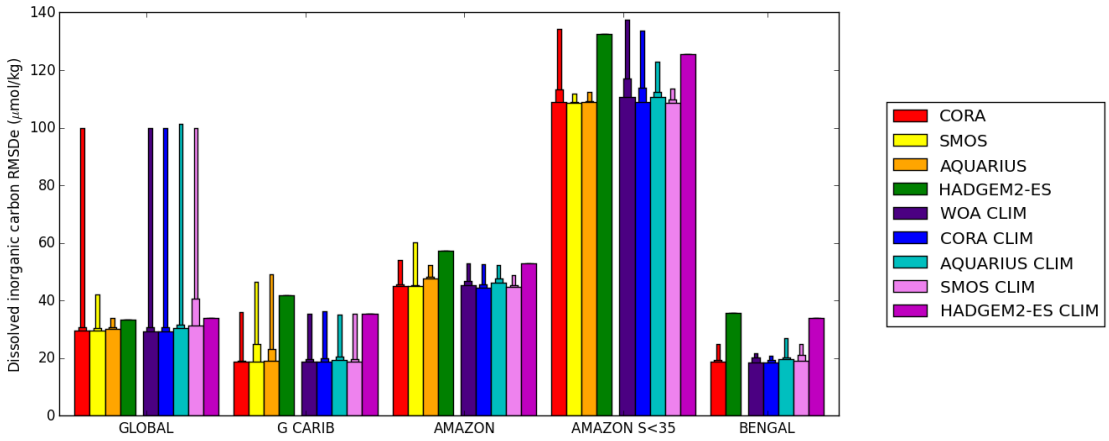

Figure 1: Estimated regional weighted RMSD (RMSDe) for each SSS source. Data are grouped by region, then by whether the input data are climatological (left group) or monthly (right group), then by SSS source. All regional output s using a given SSS source are considered, and the wide bar shows the lowest RMSDe of these, the half-width bar shows the median RMSDe and the thin bar shows the highest RMSDe. SSS sources in each group are shown in order of global lowest RMSDe. (A) A_T results; (B) C_T results.

765

766

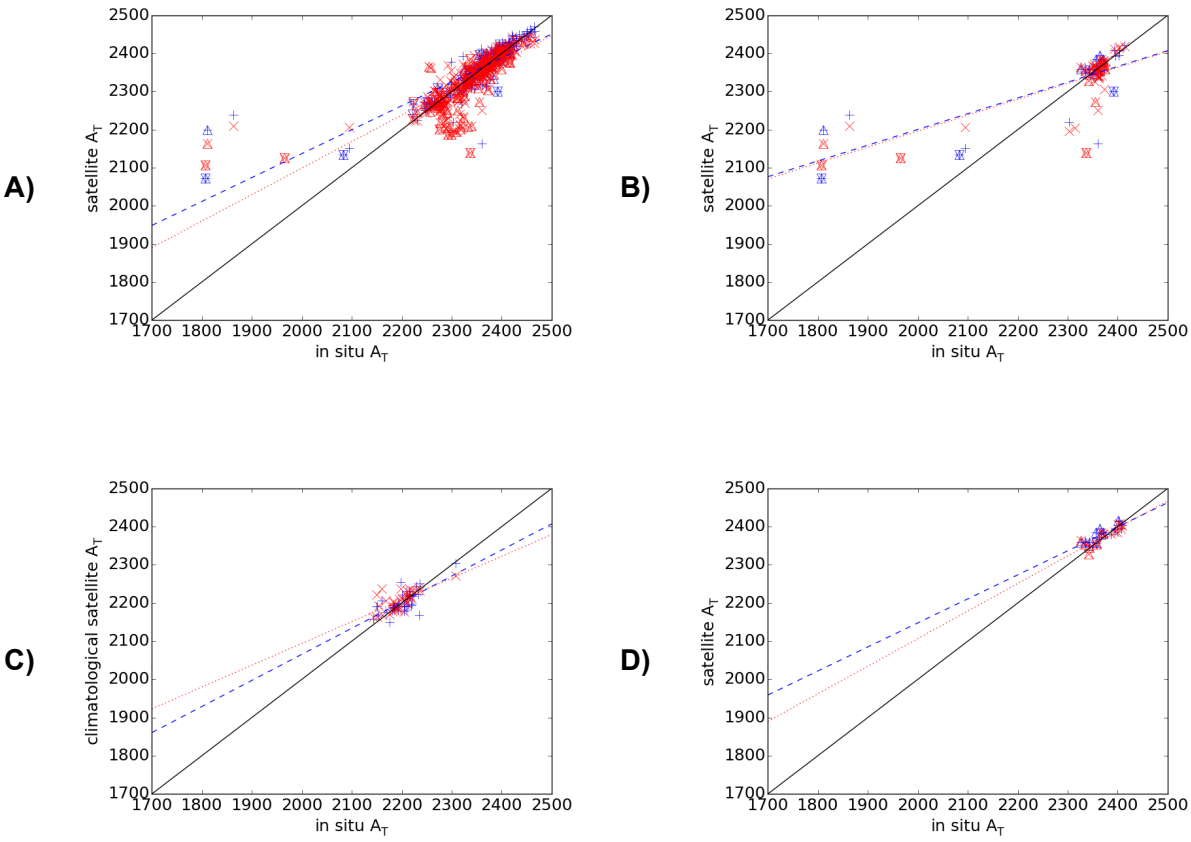

Figure 2: Comparison of A_T estimated using monthly satellite SSS with *in situ* measured A_T. (A) global; (B) Amazon plume; (C) Bay of Bengal using climatological satellite SSS; (D) Greater Caribbean. The algorithm is (Takahashi et al. 2013) with climatological WOA nitrate. Red crosses use SMOS SSS, blue plusses use Aquarius. Points with down-pointing triangles have depth less than 500 m, those with up-pointing triangles are less than 300 km from the nearest coast. Regressions use all data.

767

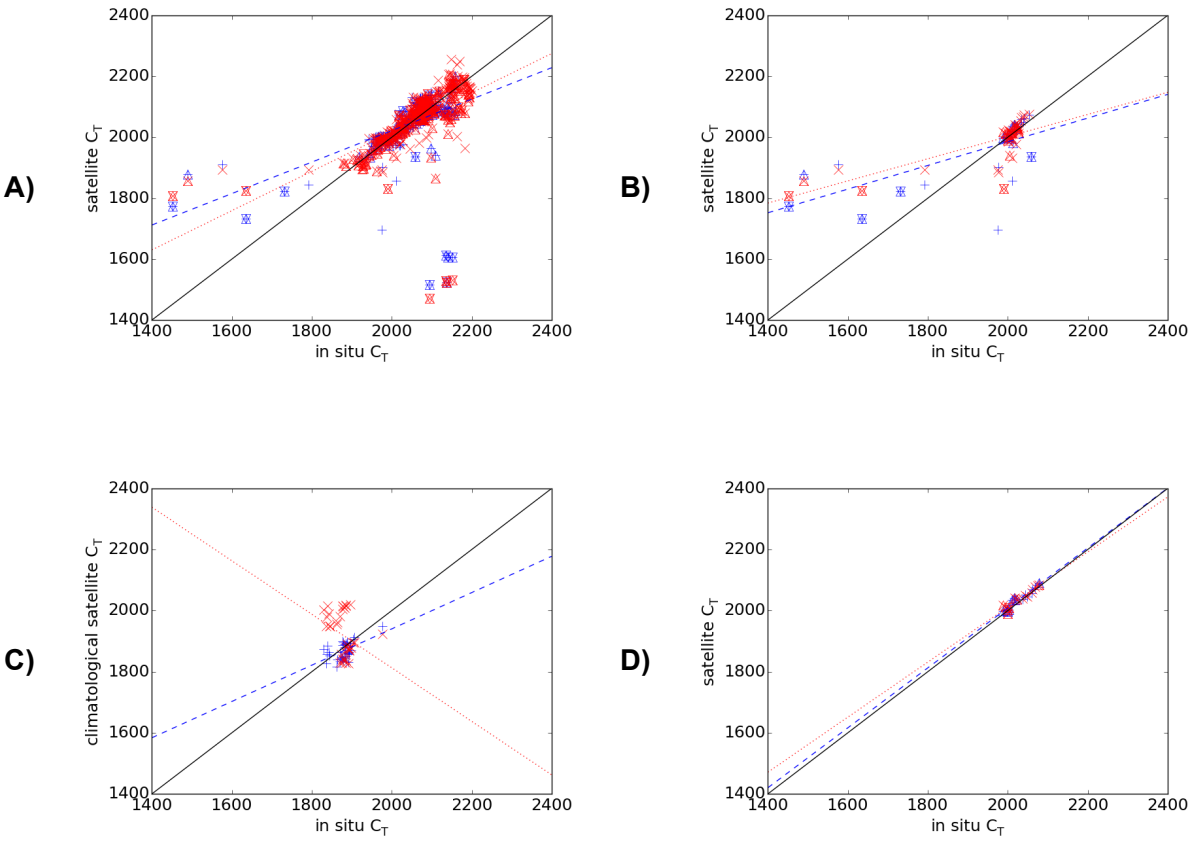

Figure 3: Comparison of C_T estimated using monthly satellite SSS with in situ measured C_T. (A) global; (B) Amazon plume; (C) Bay of Bengal using climatological satellite SSS; (D) Greater Caribbean. The algorithm is (Lee et al. 2000) with climatological WOA SST and nitrate. Red crosses use SMOS SSS, blue plusses use Aquarius. Points with down-pointing triangles have depth less than 500 m, those with up-pointing triangles are less than 300 km from the nearest coast. Regressions use all data.

768

769

770

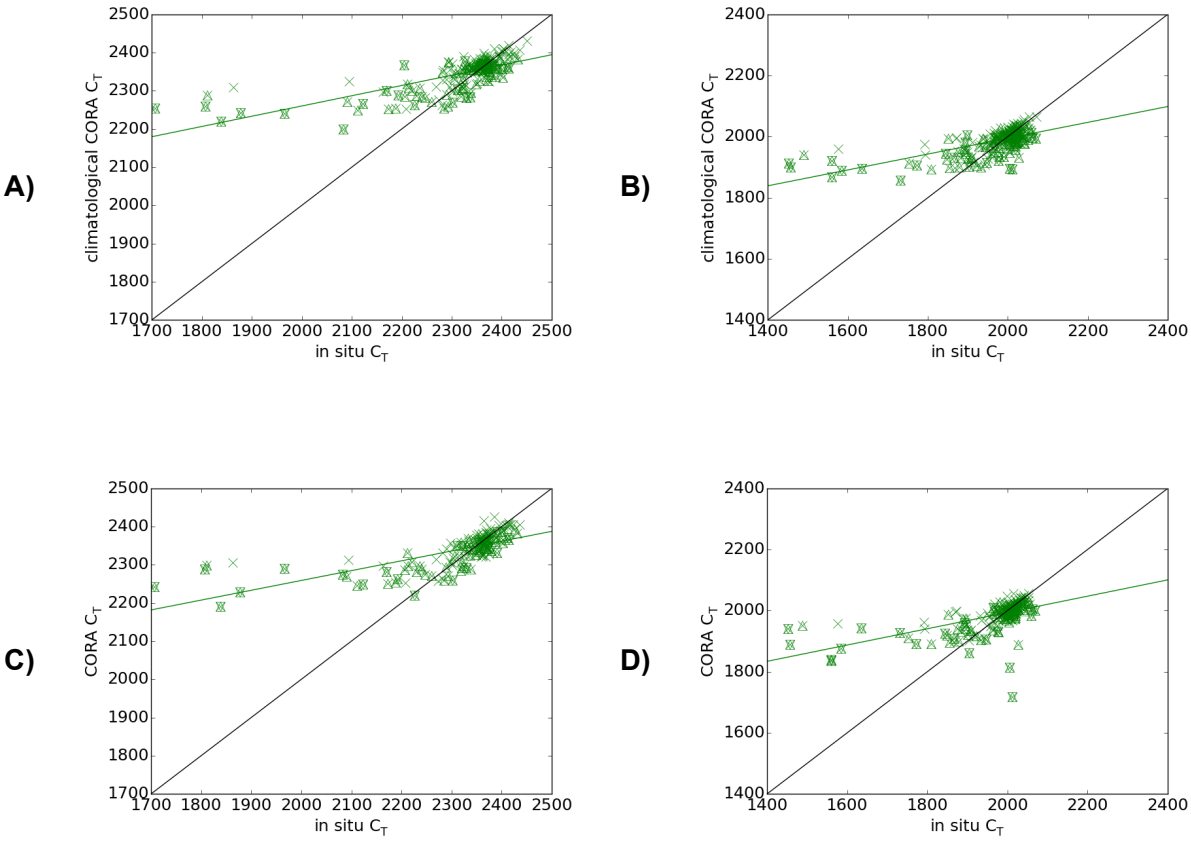

Figure 4: Comparison of A_T and C_T estimated from CORA (interpolated *in situ*) SSS with *in situ* measured values in the Amazon plume. (A) A_T comparison using climatological CORA SSS; (B) C_T comparison using climatological CORA SSS; (C) A_T comparison using monthly CORA SSS; (D) C_T comparison using monthly CORA SSS. The A_T algorithm is (Takahashi et al. 2013) with climatological WOA nitrate, and the C_T algorithm is (Lee et al. 2000) with climatological CORA SST and climatological WOA nitrate. Points with down-pointing triangles have depth less than 500 m, those with up-pointing triangles are less than 300 km from the nearest coast. Regressions use all data.

771

772

773

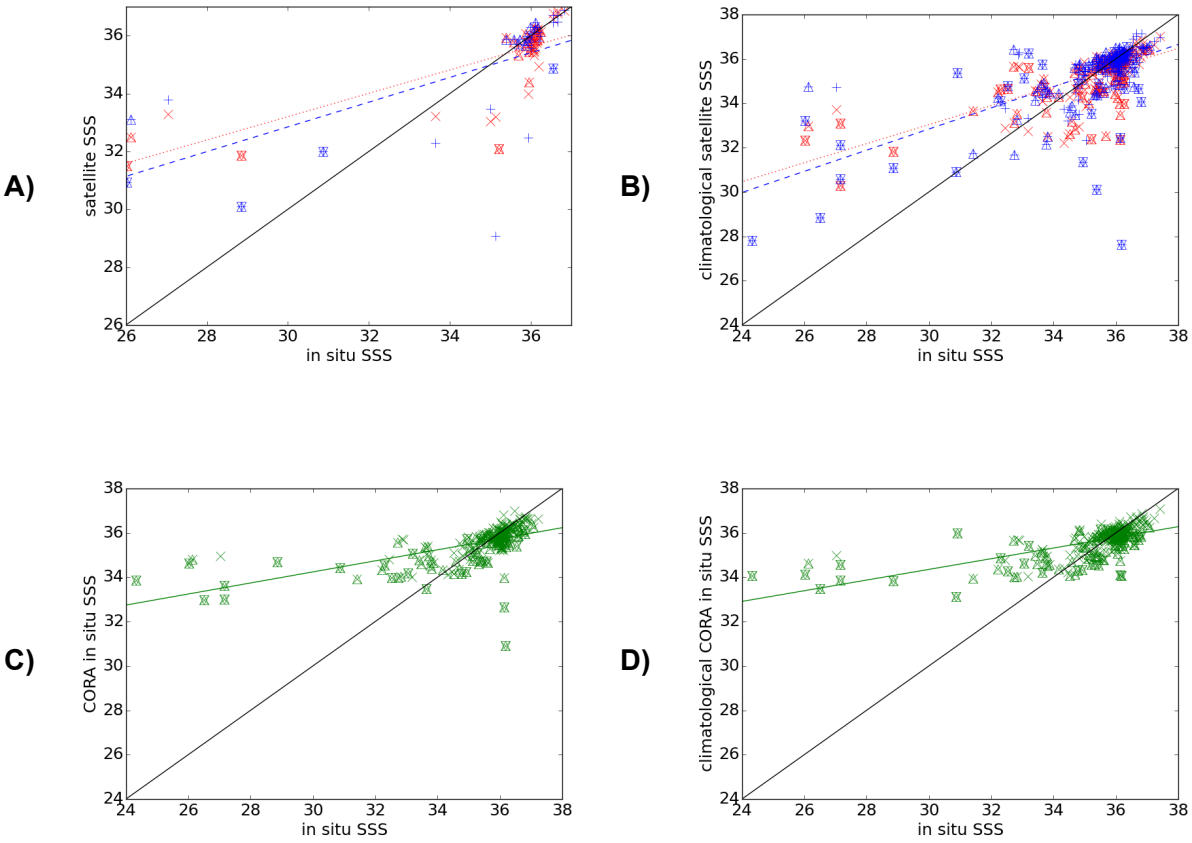

Figure 5: Comparison of satellite and CORA SSS with *in situ* measured SSS in the Amazon plume. (A) monthly SMOS (red crosses) and Aquarius (blue plusses); (B) climatological SMOS and Aquarius; (C) monthly CORA; (D) climatological CORA. Points with down-pointing triangles have depth less than 500 m, those with up-pointing triangles are less than 300 km from the nearest coast. Regressions use all data.

774

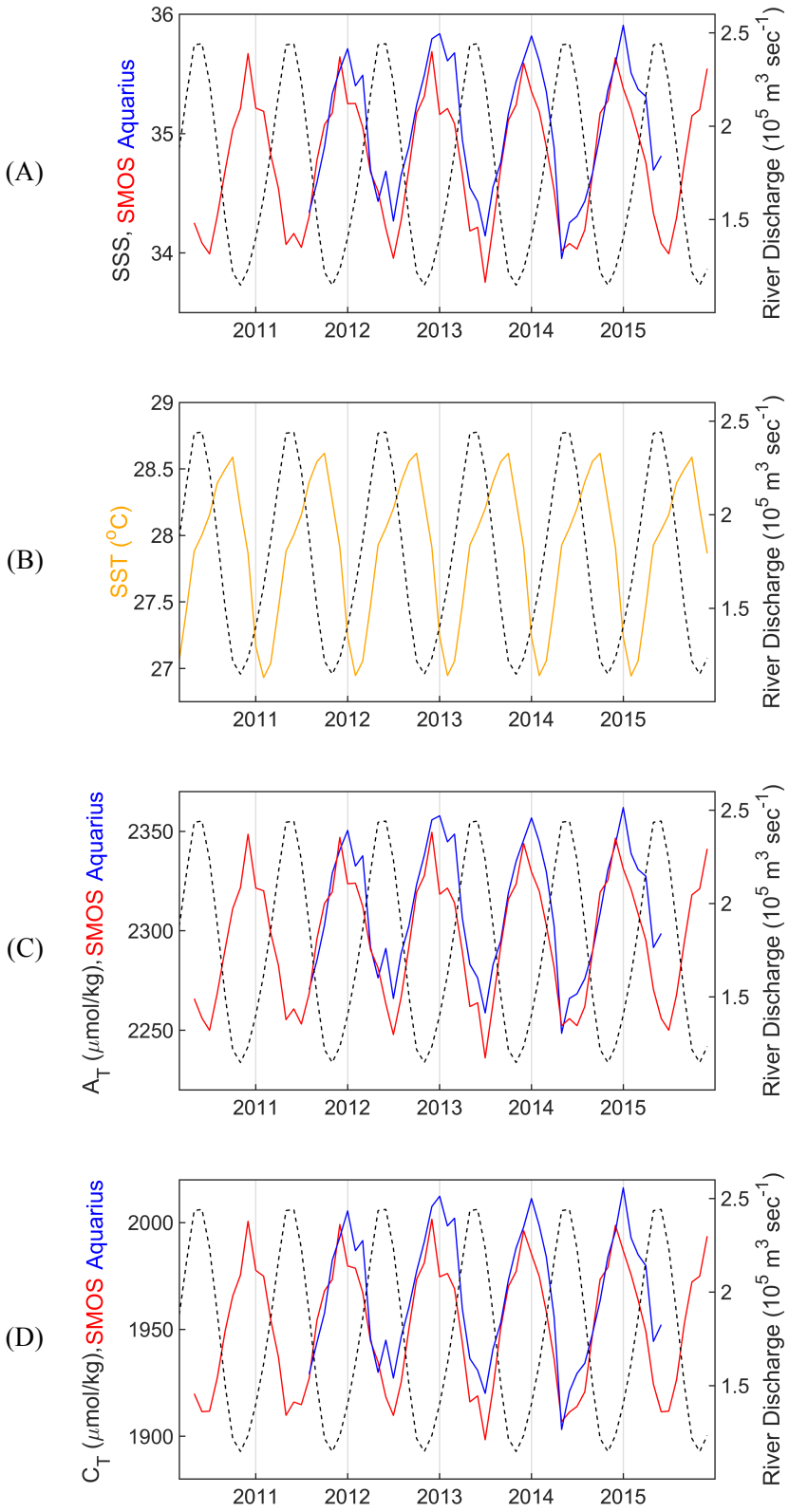

Figure 6: Time series of Amazon plume discharge and averaged satellite observations between 2010 and 2016. Monthly observations were average over the area 0°-15° N,

45°-62° W. Dashed black lines are climatological discharge at the Obidos gauge, red use SMOS SSS and blue use Aquarius SSS. In months containing both SMOS and Aquarius data, only cells with valid data in both are used. (A) monthly SMOS and Aquarius SSS; (B) climatological CORA (orange) SST; (C) A_T using the TS13 algorithm and WOA nitrate, with monthly SMOS and Aquarius SSS; (D) C_T using the L00 algorithm, CORA SST climatology and WOA nitrate, with monthly SMOS and Aquarius SSS.

775

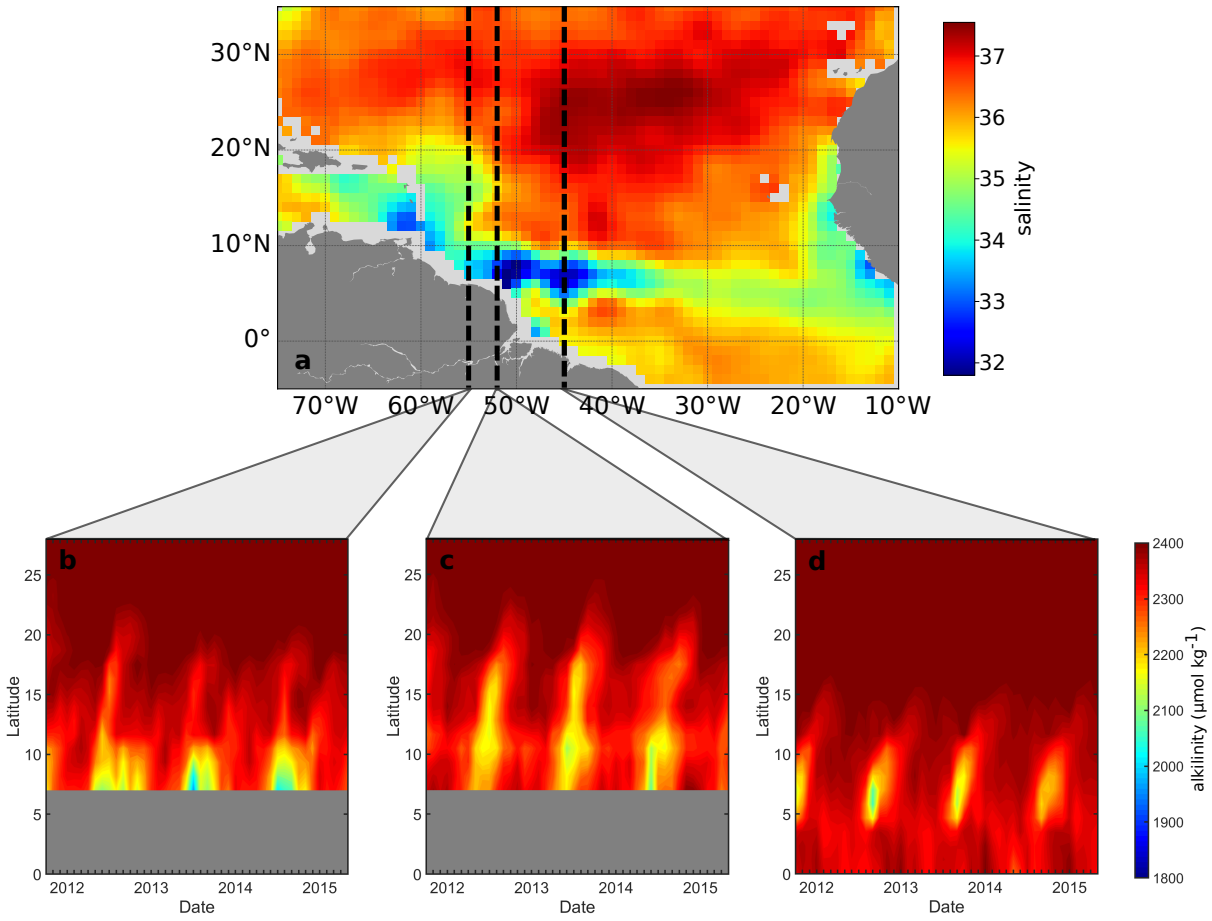

Figure 7: Aquarius derived synoptic scale observations of A_T in µmol kg^{-1} for the Amazon Plume between August 2011 and June 2015 using the TS13 algorithm and WOA nitrate, with monthly SMOS and Aquarius SSS: (a) A_T in August 2011 showing the bifurcation of the plume; (b) Hovmöller time series plot for 55° W; (c) Hovmöller time series plot for 52° W and (d) Hovmöller time series plot for 45° W.

776

777

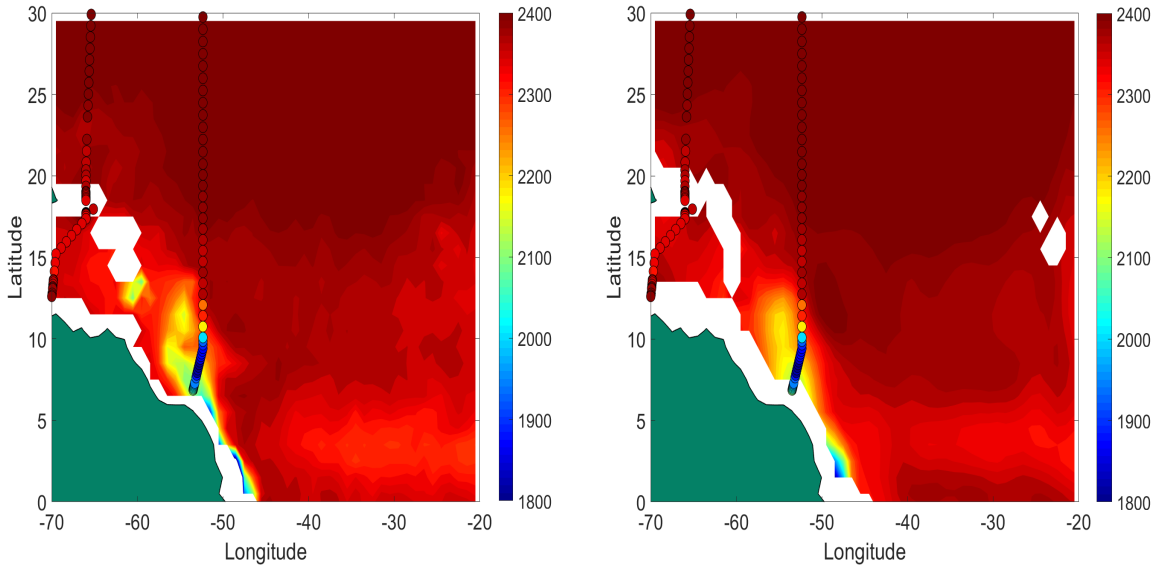

(A) (B)

Figure 8: Synoptic scale Aquarius (A) and SMOS (B) derived A_T in µmol kg^{-1} for April 2012 using the TS13 algorithm and WOA nitrate, with monthly SMOS and Aquarius SSS. *In situ* observations collected in April and May 2012 from the GLODAPv2 dataset are overlaid as circles. The May 2012 *in situ* observations are all within the offshore region (latitude >20° N).

778

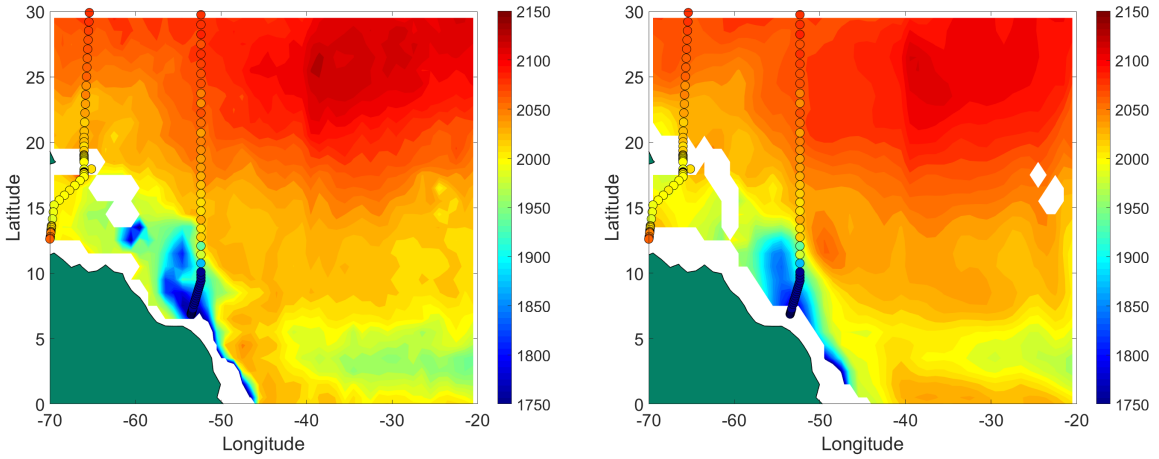

779

Figure 9: Synoptic scale Aquarius (A) and SMOS (B) derived C_T in µmol kg^{-1} for April 2012

using the L00 algorithm, CORA SST climatology and WOA nitrate, with monthly SMOS and Aquarius SSS. *In situ* observations collected in April and May 2012 from the GLODAPv2 dataset are overlaid as circles. The May 2012 *in situ* observations are all within the offshore region (latitude >20° N).

780

781 **Copyrighted material permission**

782 None required

783

784 **Supporting information/non-print material**

785 Supporting Information: Land et al., (2019) and landetal-SupportingInformation.docx

786

787 **References**

788 Akhand, A., Chanda, A., Dutta, S. Characterizing air-sea CO_2 exchange dynamics during
789 winter in the coastal water off the Hugli-Matla estuarine system in the northern Bay
790 of Bengal, India. *Journal of Oceanography* **69**, 687-697 (2013).

791 Akhand, A. *et al.* Potential CO_2 Emission Due to Loss of Above Ground Biomass from the
792 Indian Sundarban Mangroves During the Last Four Decades. *Journal of the Indian*
793 *Society of Remote Sensing*, **45**(1), 147-154 (2017).

794 Bates, N. R. *et al.* Detecting anthropogenic carbon dioxide uptake and ocean acidification in
795 the North Atlantic Ocean. *Biogeosciences* **9**, 2509-2522, doi:10.5194/bg-9-2509-2012
796 (2012).

797 BIPM, (2008) *Evaluation of measurement data – Guide to the expression of uncertainty in*
798 *measurement*, JCGM 100:2008.

Bockmon, E. E., Dickson, A. G. An inter-laboratory comparison assessing the quality of seawater carbon dioxide measurements. *Marine Chemistry* **171**, 36-43, doi:10.1016/j.marchem.2015.02.002 (2015).

Bonou, F. K., Noriega, C., Lefèvre, N., Araujo, M. Distribution of CO_2 parameters in the Western Tropical Atlantic Ocean. *Dynamics of Atmospheres and Oceans* **73**, 47-60, doi:http://dx.doi.org/10.1016/j.dynatmoce.2015.12.001 (2016).

Boutin, J., Martin, N., Reverdin, G., Yin, X., Gaillard, F. Sea surface freshening inferred from SMOS and ARGO salinity: Impact of rain. *Ocean Science* **9**, 183 (2013).

Boutin, J. *et al.* Satellite and in situ salinity: understanding near-surface stratification and subfootprint variability. *Bulletin of the American Meteorological Society* **97**, 1391-1407 (2016).

Boutin, J., Vergrly, J. L.,Marchand, S., D'Amico, F., Hasson, A., Kolodziejczyk, N., Reul, N., Reverdin, G., Vialard, J., New SMOS Sea Surface Salinity with reduced systematic errors and improved variability, *Remote Sensing of Environment*, 214, 115-134, doi:10.1016/j.rse.2018.05.022 (2018).

Brix, H., Gruber, N., Keeling, C. D. Interannual variability of the upper ocean carbon cycle at station ALOHA near Hawaii. *Global Biogeochemical Cycles* **18**, doi:10.1029/2004GB002245 (2004).

Byrne, R. H. Measuring Ocean Acidification: New Technology for a New Era of Ocean Chemistry. *Environmental Science and Technology*, 48(10), 5352−5360 (2014).

Cabanes, C. *et al.* The CORA dataset: validation and diagnostics of in-situ ocean temperature and salinity measurements. *Ocean Science* **9**, 1-18, doi:10.5194/os-9-1-2013 (2013).

Cai, W.-J. *et al.* Alkalinity distribution in the western North Atlantic Ocean margins. *Journal of Geophysical Research: Oceans* **115**, n/a-n/a, doi:10.1029/2009JC005482 (2010).

823 Caldeira, K. and Wickett, M. E., Ocean model predictions of chemistry changes from carbon
824 dioxide emissions to the atmosphere and ocean. *Journal of Geophysical Research-*
825 *Oceans*, doi: 10.1029/2004JC002671 (2005).
826 Cooley, S. R., Coles, V. J., Subramaniam, A., Yager, P. L. Seasonal variations in the Amazon
827 plume-related atmospheric carbon sink. *Global Biogeochemical Cycles* **21**, n/a-n/a,
828 doi:10.1029/2006GB002831 (2007).
829 Chao, Y., Farrara, J. D., Schumann, G., Andreadis, K. M., Moller, D. Sea surface salinity
830 variability in response to the Congo River discharge. *Continental Shelf Research* **99**,
831 35-45 (2015).
832 Choudhury, A. K., Das, M., Philip, P., Bhadury, P. An assessment of the implications of
833 seasonal precipitation and anthropogenic influences on a mangrove ecosystem using
834 phytoplankton as proxies. *Estuaries and Coasts* **38**, 854-872 (2015).
835 Del Vecchio, R., Subramaniam, A. Influence of the Amazon River on the surface optical
836 properties of the western tropical North Atlantic Ocean. *Journal of Geophysical*
837 *Research: Oceans* **109** (2004).
838 Dickson, A. G., Sabine, C. L., Christian, J. R. Guide to best practices for ocean CO_2
839 measurements, PICES Special Publication. (North Pacific Marine Science
840 Organization, 2007).
841 Drucker, R., Riser, S. C. Validation of Aquarius sea surface salinity with Argo: Analysis of
842 error due to depth of measurement and vertical salinity stratification. *J. Geophys. Res.*
843 *Oceans* **119**, 4626-4637 (2014).
844 Fine, R. A., Willey, D. A. Millero, F. J. Global variability and changes in ocean total
845 alkalinity from Aquarius satellite data, *Geophysical Research Letters*, 44, 261–267,
846 doi:10.1002/2016GL071712 (2017).

847 Friis, K., Körtzinger, A., Wallace, D. W. R. The salinity normalization of marine inorganic
848 carbon chemistry data. *Geophysical Research Letters* **30**, doi:10.1029/2002GL015898
849 (2003).
850 Ganguly, D. *et al.* Coupled micrometeorological and biological processes on atmospheric
851 CO_2 concentrations at the land–ocean boundary, NE coast of India. *Atmospheric*
852 *Environment* **45**, 3903–3910 (2011).
853 Garcia, H. E. *et al.* World Ocean Atlas 2009, Volume 4: Nutrients (Phosphate, Nitrate,
854 Silicate), NOAA Atlas NESDIS 71, edited by S. Levitus. *US Gov. Print. Off.,*
855 *Washington, DC*, 398 pp (2010).
856 Gledhill, D. K., Wanninkhof, R., Millero, F. J., Eakin, M. Ocean acidification of the greater
857 Caribbean region 1996–2006. *Journal of Geophysical research* **113**, C10031,
858 doi:10/1029/2007JC004629 (2008).
859 Gledhill, D. K., Wanninkhof, R., Eakin, C. M. Observing ocean acidification from space.
860 *Oceanography* **22** (2009).
861 International Hydrographic Organization. *Limits of oceans and seas, Special Publication 23*.
862 3 edn, (International Hydrographic Organization, 1953).
863 Ibánhez, J. S. P., Araujo, M., Lefèvre, N. The overlooked tropical oceanic CO_2 sink.
864 *Geophysical Research Letters* **43**, 3804-3812 (2016).
865 Jiang, Z. P., Tyrrell, T., Hydes, D. J., Dai, M., Hartman, S. E. Variability of alkalinity and the
866 alkalinity-salinity relationship in the tropical and subtropical surface ocean. *Global*
867 *Biogeochemical Cycles* **28**, 729-742 (2014).
868 Johnson, K.S., J.N. Plant, L.J. Coletti, H.W. Jannasch, C.M. Sakamoto, S.C. Riser, D.D.
869 Swift, N.L. Williams, E. Boss, N. Haëntjens, L.D. Talley, J.L. Sarmiento. J.
870 Biogeochemical sensor performance in the SOCCOM profiling float array,
871 *Geophysical Research-Oceans*, 122, 6416–6436. doi: 10.1002/2017JC012838 (2017).

872 Jones, C. D. *et al.* The HadGEM2-ES implementation of CMIP5 centennial simulations.
873 *Geoscientific Model Development* **4**, 543-570, doi:10.5194/gmd-4-543-2011 (2011).
874 Kroeker, K. J. *et al.* Impacts of ocean acidification on marine organisms: quantifying
875 sensitivities and interaction with warming. *Glob Chang Biol* **19**, 1884-1896,
876 doi:10.1111/gcb.12179 (2013).
877 Land, P. E. *et al.* Salinity from space unlocks satellite-based assessment of ocean
878 acidification. *Environmental science & technology* **49**, 1987-1994,
879 doi:10.102/es504849s (2015).
880 Land, P. E., Findlay, H. S., Shutler, J. D., Ashton, I. G. C., Grouazel, A., Girard-Ardhuin, F.,
881 Reul, N., Piolle, J.–F., Chapron, B., Quilfen, Y., Bellerby, R. G. J., Bhadury, P.,
882 Salisbury, J., Vandemark, D., Sabia, R., Results and analysis of oceanic total
883 alkalinity and dissolved inorganic carbon estimated from space borne, interpolated in
884 situ, climatological and Earth system model data. *PANGAEA*,
885 doi:10.1594/PANGAEA.898115 (2019).
886 Lagerloef, G., Kao, H. Y., Meissner, T., Vazquez, J. Aquarius salinity validation analysis;
887 data version 4.0. *Earth Space Res., Seattle, WA, USA* (2015).
888 Lee, K. *et al.* Global relationships of total alkalinity with salinity and temperature in surface
889 waters of the world's oceans. *Geophysical Research Letters* **33** (2006).
890 Lee, K., Wanninkhof, R., Feely, R. A., Millero, F. J., Peng, T. H. Global relationships of total
891 inorganic carbon with temperature and nitrate in surface seawater. *Global*
892 *Biogeochemical Cycles* **14**, 979-994 (2000).
893 Lefèvre, N., Diverrès, D., Gallois, F. Origin of CO_2 undersaturation in the western tropical
894 Atlantic. *Tellus B* **62**, 595-607, doi:10.1111/j.1600-0889.2010.00475.x (2010).

895 Lentz, S. J., Limeburner, R. The Amazon River Plume during AMASSEDS: Spatial
896 characteristics and salinity variability. *Journal of Geophysical Research: Oceans* **100**,
897 2355-2375 (1995).
898 Le Vine, D. M. *et al.* Aquarius: Status and recent results. *Radio Science* **49**, 709-720,
899 doi:10.1002/2014RS005505 (2014).
900 Merchant, C. J. *et al.* A 20 year independent record of sea surface temperature for climate
901 from Along-Track Scanning Radiometers. *Journal of Geophysical Research: Oceans*
902 *(1978–2012)* **117** (2012).
903 Merchant, C. J. *et al.* Sea surface temperature datasets for climate applications from Phase 1
904 of the European Space Agency Climate Change Initiative (SST CCI). *Geoscience*
905 *Data Journal* **1**, 179-191 (2014).
906 Millero, F. J., Lee, K., Roche, M. Distribution of alkalinity in the surface waters of the major
907 oceans. *Marine Chemistry* **60**, 111-130 (1998).
908 Olsen, A. *et al.* The Global Ocean Data Analysis Project version 2 (GLODAPv2) – an
909 internally consistent data product for the world ocean. *Earth System Science Data* **8**,
910 297-323, doi:10.5194/essd-8-297-2016 (2016).
911 Osterman, G.B., Eldering, A., Avis, C., Chafin, B., O'Dell, C.W., Frankenberg, C., Fisher,
912 B.M., Mandrake, L., Wunch, D., & Granat, R. Orbiting Carbon Observatory-2 (OCO-
913 2) data product user's guide, operational L1 and L2 data versions 7 and 7R. *Jet*
914 *Propulsion Laboratory, Pasadena, CA, USA* (2016).
915 Perry, G. D., Duffy, P. B., Miller, N. L. An extended data set of river discharges for
916 validation of general circulation models. *Journal of Geophysical Research:*
917 *Atmospheres* **101**, 21339-21349 (1996).
918 Raven, J. A., Caldeira, K., Elderfield, H., Hoegh-Guldberg, O., Liss, P. S., Riebesell, U., et

al. Ocean acidification due to increasing atmospheric carbon dioxide, *The Royal Society,* Policy document 12/05 (2005).

Reul, N. and Team, I. C.-C. *SMOS Level 3 and 4 Research products of the Centre d'Expertise Ifremer du CATDS -Algorithm Theoretical Background Document, IFREMER-CNES technical document 2015*, <https://www.catds.fr/> (2015).

Reul, N. *et al.* Overview of the first SMOS sea surface salinity products. Part I: Quality assessment for the second half of 2010. *IEEE Transactions on Geoscience and Remote Sensing* **50**, 1636-1647 (2012).

Reul, N. *et al.* Sea surface salinity observations from space with the SMOS satellite: A new means to monitor the marine branch of the water cycle. *Surveys in Geophysics* **35**, 681 (2014).

Salisbury, J. *et al.* Spatial and temporal coherence between Amazon River discharge, salinity, and light absorption by colored organic carbon in western tropical Atlantic surface waters. *Journal of Geophysical Research: Oceans* **116** (2011).

Salisbury, J. *et al.* How Can Present and Future Satellite Missions Support Scientific Studies that Address Ocean Acidification? *Oceanography* **28**, 108-121, doi:10.5670/oceanog.2015.35 (2015).

Samanta, S., Dalai, T. K., Pattanaik, J. K., Rai, S. K., Mazumdar, A. Dissolved inorganic carbon (DIC) and its δ 13 C in the Ganga (Hooghly) River estuary, India: Evidence of DIC generation via organic carbon degradation and carbonate dissolution. *Geochimica et Cosmochimica Acta* **165**, 226-248 (2015).

Santana-Casiano, J. M., González-Dávila, M., Rueda, M. J., Llinás, O., González-Dávila, E. F. The interannual variability of oceanic CO_2 parameters in the northeast Atlantic subtropical gyre at the ESTOC site. *Global Biogeochemical Cycles* **21**, doi:10.1029/2006GB002788 (2007).

944 Sarma, V. V. S. S. *et al.* Sources and sinks of CO_2 in the west coast of Bay of Bengal. *Tellus*
945 *B* **64**, 10961, doi:10.3402/tellusb.v64i0.10961 (2012).
946 Sarmiento, J. L., Gruber, N. *Ocean biogeochemical dynamics*. (Cambridge University Press,
947 2006).
948 Sasse, T.P., McNeil, B.I., Abramowitz, G. A novel method for diagnosing seasonal to inter-annual
949 surface ocean carbon dynamics from bottle data using neural networks. *Biogeosciences* **10**,
950 4319 (2013).
951 Smith, S. V., Key, G. S. Carbon dioxide and metabolism in marine environments. *Limnol.*
952 *Oceanogr* **20**, 493-495 (1975).
953 Takahashi, T. *et al.* Climatological mean and decadal change in surface ocean pCO_2, and net
954 sea–air CO_2 flux over the global oceans. *Deep-Sea Res. Pt II* **56**, 554-577,
955 doi:10.1016/j.dsr2.2008.12.009 (2009).
956 Takahashi, T., Sutherland, S. Climatological mean distribution of pH and carbonate ion
957 concentration in Global Ocean surface waters in the Unified pH scale and mean rate
958 of their changes in selected areas. Report No. OCE 10-38891, (National Science
959 Foundation, Washington, D. C., USA, 2013).
960 Taylor, An introduction to Error Analysis The study of uncertainties in physical
961 measurements, *University Science Books*, second edition, 1997.
962 Ternon, J. F., Oudot, C., Dessier, A., Diverres, D. A seasonal tropical sink for atmospheric
963 CO_2 in the Atlantic ocean: the role of the Amazon River discharge. *Marine Chemistry*
964 **68**, 183-201, doi:http://dx.doi.org/10.1016/S0304-4203(99)00077-8 (2000).
965 Yang, D., Liu, Y., Cai, Z., Chen, X., Yao, L., Lu, D. First Global Carbon Dioxide Maps
966 Produced from TanSat Measurements, *Advances in Atmospheric Sciences*, doi:
967 10.1007/s00376-018-7312-6 (2018).